

**MICRO AND NANO FLUIDICS FOR DNA MOLECULES  
APPLICATIONS**

**BIKKAROLLA SANTOSH KUMAR  
(M.Sc, UOH)**

**A THESIS SUBMITTED  
FOR THE DEGREE OF MASTER OF SCIENCE BY RESEARCH  
DEPARTMENT OF PHYSICS  
NATIONAL UNIVERSITY OF SINGAPORE**

**2011**

## **Abstract**

In chapter 1, we summarize the properties of nucleic acids in bulk and in nano-confinement. We will be discussing the conformation of DNA in the presence of condensing ligands spermidine, cobalt hexamine and spermine.

In chapter 2, we describe the materials and methods used in the experiments. We will describe the procedure for the fabrication of micro-fluidics channels in SU-8, fabrication of a nano-micro fluidic chip in PDMS (Polydimethylsiloxane), injecting molecules in nano-channels, and fluorescence imaging of T4-DNA molecules in nano-channels.

In chapter 3 our main interest is to study the conformation of T4 DNA molecule in the presence multivalent cations like spermidine, cobalthexamine and spermine. To observe the conformation of dye labeled T4 DNA molecule we used fluorescence microscope. Our results show that transition from elongated state to collapsed state is discrete. The critical concentration of the cation needed to condense the DNA molecule is lowest for the tetravalent cation and highest for the trivalent cation. The co-existence region is larger for trivalent cation and less for the tetravalent cation

In chapter 4 we aim to study the equilibrium conformation of the DNA molecule in nanoconfinement. For this purpose we fabricated nano-channels of 200nm in width and 300nm in height in PDMS and used fluorescence microscope to observe the elongation of the molecule. Our results show that in 1XT buffer (10mM Tris-Hcl pH=8.5) the elongation of T4 DNA molecule is around 12 $\mu$ m

In chapter 5, we demonstrate the integration of the PDMS micro-fluidic channel with graphene device as a novel way to achieve electrolyte top gating of graphene. By applying a back gate voltage, carrier concentrations of up to  $2.3 \times 10^{12} /\text{cm}^2$  and mobility values of up to  $7500\text{cm}^2/\text{Vs}$  can be obtained in the device at ambient conditions. In the case of electrolyte top gating, significantly higher doping concentrations can be achieved as compared to conventional back gating at low voltages. The effective implementation of electrolyte top gating by using micro channels serves as a compelling proof of concept that graphene can be used as a chemical and biological sensor.

## **Acknowledgements**

I would also like to thank everyone in Johan's Laboratory group and Jeroen's Laboratory group who helped me along the way, especially Dr. P.G. Shao who gave me lots of practical advice. Thanks to my friends and family who helped me get here. Finally, I want to thank the person who guided me through my research - my advisor Assoc.Prof. Johan van der Maarel.

## **Contents**

<b>Abstract.....</b>	<b>2</b>
<b>Acknowledgements.....</b>	<b>4</b>
<b>List of figures.....</b>	<b>8</b>

### **Chapter 1 Introduction to physics of nucleic acids**

<b>1.1 The ideal chain model.....</b>	<b>11</b>
<b>1.2 Flory model of volume exclusion.....</b>	<b>13</b>
<b>1.3 Conformation of DNA and its biological meaning.....</b>	<b>15</b>
<b>1.4 Introduction to polyamines.....</b>	<b>18</b>
<b>1.5 De Gennes Blob model for confined polymers.....</b>	<b>20</b>
<b>1.6 Introduction to micro- and nanochannel devices.....</b>	<b>22</b>
<b>1.7 Conformation of molecule in the nano-confinement.....</b>	<b>24</b>
<b>1.8 References.....</b>	<b>26</b>

### **Chapter 2 Materials and method**

<b>2.1 Introduction to YOYO-1 and DAPI.....</b>	<b>28</b>
<b>2.2 DNA sample preparation.....</b>	<b>28</b>
<b>2.3 Fabrication of micro and nano-channels.....</b>	<b>30</b>
<b>2.4 Fabrication of micro channels.....</b>	<b>32</b>
<b>2.5 Fabrication of nano channels.....</b>	<b>32</b>
<b>2.6 Transfer of nano-micro structures to PDMS.....</b>	<b>33</b>
<b>2.7 Air plasma treatment.....</b>	<b>33</b>
<b>2.8 Injecting molecules into nano-channels.....</b>	<b>35</b>
<b>2.9 Florescence imaging of T4 DNA molecules in nano-channels.....</b>	<b>36</b>

2.10

References.....37

### **Chapter 3 Effect of polyamines on the conformation of DNA**

3.1 Abstract.....38

3.2 Introduction.....38

3.3 Fragmentation of DNA molecules with incident light.....40

3.4 Condensation of DNA observed with fluorescence microscope.....41

3.5 The Conformation of DNA in the presence condensing ligands .....42

    3.5.1 Folding transition of T4 DNA in the presence of spermidine.....42

    3.5.2 Folding transition of T4 DNA in the presence of cohex.....45

    3.5.3 Folding transition of T4 DNA in the presence of spermine.....47

3.6 Effect of fluorescence dye on the conformation of DNA molecule.....48

3.7 DNA concentration effects.....51

3.8 Conclusion.....54

3.9 References.....55

### **Chapter 4 DNA in nano-channels**

4.1 Abstract.....58

4.2 Extensions of T4 DNA molecules in nano-channels.....58

4.3 Translocation of T4 DNA molecules nano-channels.....62

4.4 Cross section of micro channels.....66

4.5 Cross section of nano-channels.....70

4.6 Conclusion.....71

4.7 References.....72

**Chapter 5 Electrolyte top gating of graphene by using micro fluidic channel**

5.1	Abstract.....	74
5.2	Introduction.....	74
5.3	Device fabrication and measurement.....	75
5.4	Back gating.....	79
5.5	Top gating using DI water.....	83
5.6	Future work.....	84
5.7	Conclusion.....	87
5.8	References.....	88

## List of figures

<b>Fig.1: (a) A schematic diagram of the chromosome in the eukaryotic cell. (b) The structure of nucleosome with an electron micrograph. ....</b>	<b>15</b>
<b>Fig.2: The donut or the stem structure of T4 or T7 DNA induced by poly (ethylene oxide) and polylysine.....</b>	<b>16</b>
<b>Fig.3: (a) A schematic diagram of DNA structure. (b) The base pair formed by purines and pyrimidines in nucleotide.....</b>	<b>17</b>
<b>Fig.4: The binding model of spermidine in DNA. (a) The chemical structure of spermidine. (b) Spermidine binds three phosphates adjacent from the same strand. (c) Intrastrand across the major groove. (d) Intrastrand across the minor groove. ....</b>	<b>19</b>
<b>Fig.5: De Gennes “Blob” model.....</b>	<b>20</b>
<b>Fig.6: DNA molecule in various confinements.....</b>	<b>25</b>
<b>Fig.7: Coil and globule state of the DNA molecule.....</b>	<b>30</b>
<b>Fig.8: Fabrication of nano-micro structures.....</b>	<b>31</b>
<b>Fig.9: Nano-micro fluidic chips.....</b>	<b>34</b>
<b>Fig.10: Fluorescence damage of DNA molecules.....</b>	<b>41</b>
<b>Fig.11: Fluorescence damage of the DNA molecule with 400<math>\mu</math>M of spermidine... </b>	<b>41</b>
<b>Fig.12: Brownian motion of the DNA molecule.....</b>	<b>42</b>
<b>Fig.13: Coil and globule state of the DNA molecule.....</b>	<b>42</b>
<b>Fig.14: Histograms showing the distribution of the conformation of the YOYO-1-DNA molecules with various concentrations of spermidine.....</b>	<b>44</b>
<b>Fig.15: Phase diagram showing the different states of the DNA molecule with increasing concentration of spermidine.....</b>	<b>44</b>
<b>Fig.16: Histograms showing the distribution of the conformation of YOYO-1-DNA molecules with various concentrations of cohex.....</b>	<b>46</b>



<b>Fig.17: Phase diagram showing the different states of YOYO-1-DNA molecule with increasing concentration of cohex.....</b>	<b>46</b>
<b>Fig.18: Histograms showing the distribution of the conformation of YOYO-1-DNA molecules with various concentrations of spe.....</b>	<b>47</b>
<b>Fig.19: Histograms showing the distribution of the conformation of DAPI-DNA molecules with various concentrations of spermidine.....</b>	<b>49</b>
<b>Fig.20: Phase diagram showing the different states of DAPI-DNA molecule with increasing concentration of spermidine.....</b>	<b>49</b>
<b>Fig. 21:a) Fluorescence image of T4 DNA at various DNA concentrations b)Phase diagrams for a) conc of bp= 0.1<math>\mu</math>M b) Conc of bp= 1<math>\mu</math>M c) conc of bp=5<math>\mu</math>M .....</b>	<b>52</b>
<b>Fig.22: DNA molecule confined in a channel of diameter.....</b>	<b>60</b>
<b>Fig.23:Extension of T4 DNA molecules in 1XT buffer system confined in 200nmX300nm PDMS nano-channels.....</b>	<b>61</b>
<b>Fig.24:Single T4 DNA molecules confined in 200nmX300nm channels.....</b>	<b>62</b>
<b>Fig.25: Sequence of deinterlaced video images showing the passage of a T4-DNA molecule (circled) through a nanochannel.....</b>	<b>63</b>
<b>Fig.26: Graph of velocity vs. field strength.....</b>	<b>66</b>
<b>Fig.27: Captured frames showing the DNA length at different applied potentials, hence velocities. a) applied potential of 2.5V b) applied potential of 3.0V and c) applied potential of 4.5V.....</b>	<b>67</b>
<b>Fig. 28: Optical image of cross section of 8-micron width channel.....</b>	<b>67</b>
<b>Fig.29: I-V characteristic of a salt solution (1 M KCl, 10 mM Tris-base, pH= 8.0) along a 8 micron width and 11.5 micro meter deep channel.....</b>	<b>67</b>
<b>Fig. 30: Optical image of cross section of 12-micron width channel.....</b>	<b>68</b>
<b>Fig.31: The I-V characteristic of a salt solution (1 M KCl, 10 mM Tris-base, pH= 8.0) along a 12 micron width and 11.5 micro meter deep channel.....</b>	<b>68</b>
<b>Fig.32: Optical image of cross section of 20-micron width channel.....</b>	<b>69</b>

**Fig.33: The I-V characteristic of a salt solution (1 M KCl, 10 mM Tris-base, pH= 8.0) along a 20 micron width and 11.5 micro meter deep channel.....69**

**Fig.34: I-V measurement of 300nmX300nm PDMS nano-channels.....70**

**Fig.35: I-V measurement of 100nmX105nm PDMS nano-channels.....71**

**Fig.36: Graphene device after integration with micro-fluidic channel.....77**

**Fig.37:Cross sectional view of electrolyte top-gated measurement device.....77**

**Fig.38: Current bias measurement layout.....78**

**Fig.39: Energy spectrum in graphene.....80**

**Fig.40: a) Resistance of the graphene with respect to the backgate voltage  
b)Mobility of the charge carriers with respect to the backgate Voltage.....82**

**Fig.41: shows the resistance of the graphene with respect to the top gate voltage from -1v to +1v.....85**

# Chapter1 Introduction to the physics of nucleic acids

## 1.1 The ideal chain model

The simplest model for a polymer represents the molecule as a sequence of identical monomers in a chain of  $N$  links. Each monomer has a center of mass at  $\vec{r}_i$ . This ideal chain has a step vector between subsequent monomers, of

$$\vec{l}_i = \vec{r}_i - \vec{r}_{i-1} \dots \dots \dots (1)$$

This describes a random walk with step length through space. Note that the orientation of one link is independent of the orientation of other links, and that there is no interaction between segments that are not directly linked; there are no long-range interactions. The contour length of the molecule is given by

$$L_c = N |\vec{l}_i| = Nl \dots \dots \dots (2)$$

The end-to-end distance of the molecule can be calculated by forming the expectation value of the squared sum of all steps

$$\langle h^2 \rangle = Nl^2 \dots \dots \dots (3)$$

This can be used to define an effective radius for the polymer coil, also called the radius of gyration (Graessley, 2008)

$$R_g = \frac{\langle h^2 \rangle^{1/2}}{\sqrt{6}} \cong \frac{N^{1/2}l}{\sqrt{6}} \dots \dots \dots (4)$$

From the Gaussian distribution of radii (not shown), an effective free energy for the molecules can be derived. The source term is completely entropic, and we find the free energy as

$$F(R) = U - TS = F_o + k_B T \frac{3R^2}{2Nl^2} \dots\dots\dots(5)$$

Here  $F_o$  is the minimum free energy and  $R$  is the radius of gyration. Note that this is a harmonic spring free energy in  $R$ , and that the spring constant is temperature dependent. For DNA, this model of freely jointed links of monomers has to be altered because neighboring base pairs are stacked, leading to a bending stiffness. DNA is thus better described by a worm-like chain (WLC). The WLC model envisions the polymer as a uniform, continuously flexible rod. The key parameter of the WLC model is the persistence length  $L_p$ , defined as the length over which the autocorrelation of the tangential vector decays to  $1/e$ . When considering the WLC, there exist two limiting considerations:  $L_C \ll L_p$ , and  $L_C \gg L_p$ . In the case of a very long chain, a detailed calculation yields a relationship between contour length and the radius of gyration as in Equation for  $R_g$ .

## 1.2 Flory model of volume exclusion

Note that the DNA worm-like chain in reality is not a “phantom chain” that can intersect itself; two links cannot occupy the same space at the same time. Flory was the first to take into account volume exclusion effects, and used the mean field approximation for the monomer concentration,

$$\langle c^2 \rangle = \langle c \rangle^2 \cong \frac{N^2}{R^6} \dots\dots\dots(6)$$

If correlations between monomers are ignored. Flory then argued that the energy due to the excluded volume could be calculated by

$$F_{Volume} = \int K_B T \chi c^2 \overline{dx}^3 \dots\dots\dots(7)$$

The parameter ‘ $\chi$ ’ is the excluded volume parameter, which has the units of volume. Onsager proposed in the context of liquid crystals that the volume occupied by two rods of length  $L_p$  and width  $w_{eff}$ , on average, could be represented as

$$\chi = w_{eff} L_p^2 \dots\dots\dots(8)$$

In the following, we will drop factors of order one, and all results serve to establish relative relationships. If we assume that the molecule is shaped as a spherical blob (“Flory coil”) with radius  $R$  with constant density throughout, we can combine the free energy of the freely jointed chain with the Flory energy to form the total free energy

$$F_{total} = F_{spring} + F_{Volume} \dots\dots\dots(9)$$

If  $N_B$  is the number of persistence lengths stored inside the blob, this becomes

$$F_{total} = K_B T \left[ \frac{R^2}{L_p^2 N_B} + \frac{L_p^2 w_{eff} N_B^2}{R^3} \right] \dots \dots \dots (10)$$

The equilibrium radius can then be found by demanding a local minimum of the free energy

$$\frac{\partial F_{Total}}{\partial R} = 0 \dots \dots \dots (11)$$

Solving for R yields the Flory radius

$$R_f = \chi^{1/5} L_p^{2/5} N^{3/5} \dots \dots \dots (12)$$

(Shaefer et al. 1980, Moon et al. 1991) for arbitrary  $\chi$ . Combining this result with Onsager's excluded volume parameter leads to a Flory coil with length of

$$R_f = (L_p w_{eff})^{1/5} L_c^{3/5} \dots \dots \dots (13)$$

### 1.3 Conformation of DNA and its biological meaning

The word conformation means the arrangement of structure. In living cells, the arrangement of deoxyribonucleic acid (DNA) is important in many aspects. For instance, the compaction of DNA in prokaryotic and eukaryotic cells [1], the mechanism of DNA-protein interaction [2], and the enzymatic reaction concerned with DNA transcription [3] are related to the conformation of DNA. Consider this example illustrating the compaction of DNA: a human DNA molecule about one meter in length can be packed into a micron-scale chromosome. Compaction of DNA to a million fold is established by the histone. A beads-on-a-string structure of DNA-histone complex (namely chromatin) is formed in the nucleosome (figure 1 (b)). This phenomenon exists exclusively in the eukaryotic cells. However in prokaryotic cells, spermidine plays a role in the compaction of DNA.

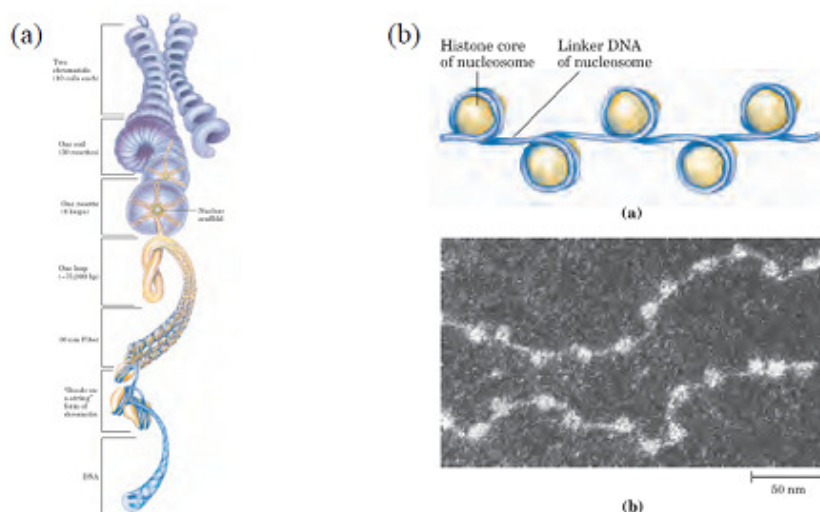


Fig (1a): A schematic diagram of the chromosome in eukaryotic cell (b) The structure of Chromosome with an electron micrograph [4] (image taken from Lehninger principle of bio-chemistry).

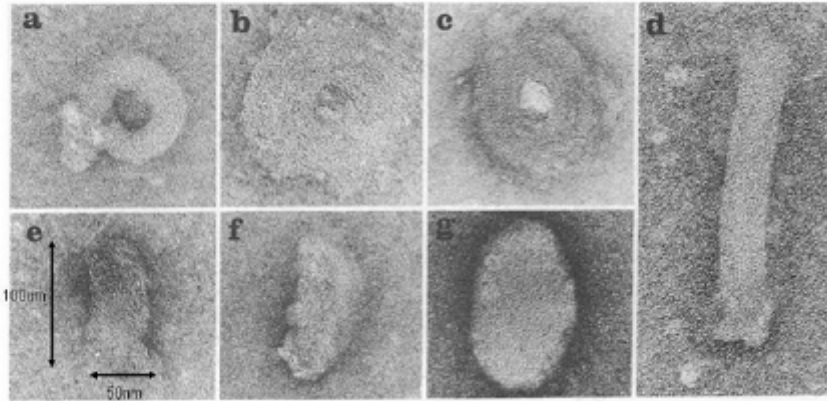


Fig (2) The donut or the stem structure of T4 or T7 DNA induced by the poly (ethylene oxide) and the polylysine [5]. [a,d] the donut or the stem structure of T7 DNA induced by the polylysine are presented. In the panel [b,c] the donut or the stem structure of T4 DNA induced by the polylysine are presented. In the panels [e,f,g] t4 DNA is collapsed with the poly(ethylene oxide). The average length and width of the poly(ethylene oxide) collapsed T4 DNA are 100nm and 50nm.(image taken from Lehninger Principles of Bio-chemistry)

Another example is the compaction of DNA in viruses. In a paper reported by U. K. Laemmli [5], the donut or the stem structures of T4 and T7 phage DNA are induced by poly(ethylene oxide) and polylysine [5] (Fig. 2). The sizes of the poly (ethylene oxide) or the polylysine collapsed DNA is slightly larger than the phage head. The mechanism of the compaction of DNA in viruses is still not clear. Another feature of these condensed structures of DNA is that the efficiency of digestion by the single-strand specific endonuclease is enhanced. It suggests that the conformational change of DNA increases the enzyme-vulnerable regions and the condensed DNA is easier to be attacked by the endonuclease. However, in other cases, the activity of the restriction endonuclease is inhibited by the presence of spermidine (SPD) and spermine [6]. It is known that the conformation of DNA is also changed in the presence of spermidine [1]. The conformational change of DNA induced by spermidine is examined in this thesis.



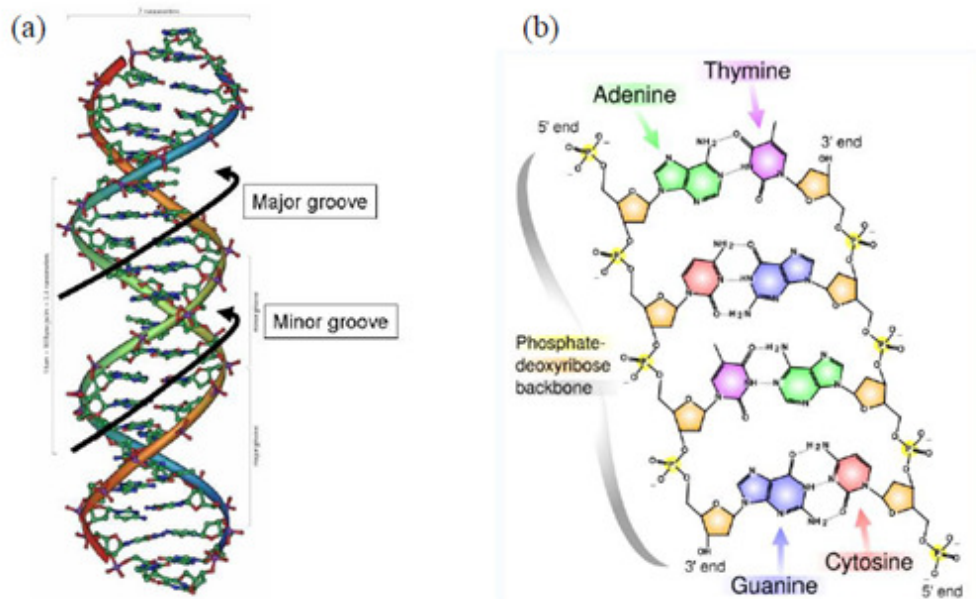


Fig (3): (a) schematic diagram of DNA structure (b) The base pairs formed by purines and pyrimidines and nucleotides [7] (image taken from wiki/DNA).

The double-helix structure of DNA was first proposed by James D. Watson and Francis Crick in 1953. The nucleotides are the monomers of DNA (figure 3). Two strands of the nucleotides forms a double-helix structure. The major groove and minor groove along the DNA structure are formed. Three major portions of the nucleotides are: the base, the deoxyribose, and the phosphate group. The four base types are adenine (abbreviated A), guanine (G), cytosine (C), and thymine (T). The hydrogen bonds between these bases are formed following the complementary base-pairing rule. The negative charge of DNA is carried by the phosphate group in the back bone. From the point of view of evolution, the specific sequence of DNA carries the information of heredity. A specific sequence of DNA, namely the gene, transcribes to the ribonucleic acid (RNA) and the RNA is translated to the functional protein. This process called Central Dogma is believed to govern the life cycle of all creatures on earth. From the point of view of polymer physics, the DNA is an extremely long molecule chain made up

of repeating nucleotides. The behavior of DNA is well described by the *Kratky-Porod* worm-like chain model (WLC) [8].

#### **1.4 Introduction to polyamines**

Putrescine, spermidine, and spermine, which are classified as polyamines, are essential to prokaryotes, eukaryotes, viruses [10], and bacteria [11]. In mammalian cells, spermidine is found in millimolar concentration. Spermidine is a trivalent cation with a molecular weight of 145 daltons and the chemical formula is  $C_7H_{19}N_3$  (figure 4 (a)). Except for the compaction of DNA, spermidine is also related to transcription, cell growth and death regulation [12]. Due to the multication feature, spermidine binds the highly negative charged DNA and it makes DNA suitable for compact packaging and folding in the cell by neutralization. The binding model of spermidine is proposed by Amin A. Ouameur et al [13]. In figure 4, spermidine binds the adjacent phosphates from the same strand (figure 4 (b)) or intrastrand across the major groove or the minor groove of DNA (figure 4 (c, d)). There is an abundant literature devoted to the studies of the conformation of DNA changes in the presence of spermidine *in vitro* [15, 16, 17]. To probe the conformation of DNA, electron microscopes and atomic force microscopes (AFM) are the most commonly used. The toroid model of forming the DNA-SPD complex has been used the most accepted model in the past decade [18]. However, the flower-shaped structure has also been reported by Ye Fang et al [17].

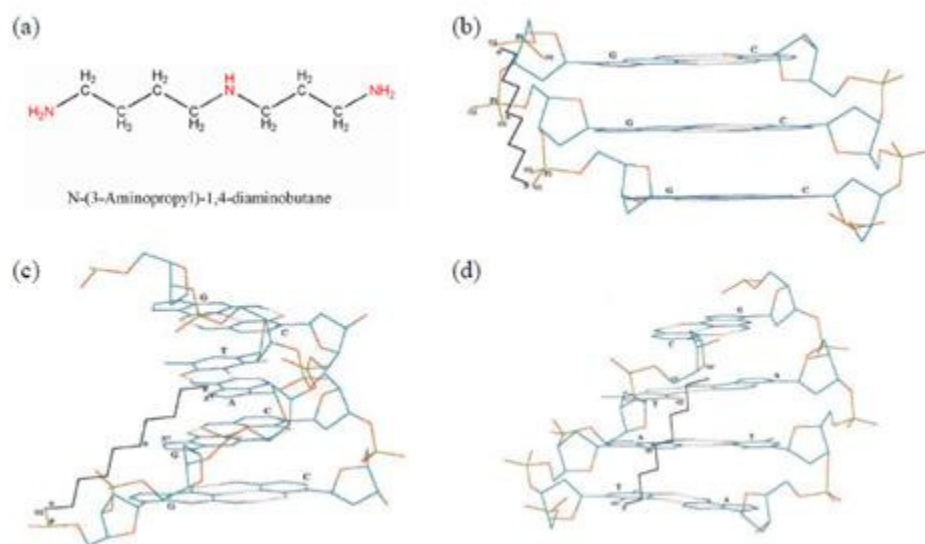


Fig (4): The binding model of spermidine in DNA.(a) The chemical structure of spermidine[14].(b) spermidine binds three phosphates adjacent from the same strand.(c) Intrastrand across the major groove.(d) Intrastrand across the minor groove[13] (image taken from Amin Ahmed Ouameur and Heidar-Ali Tajmir-Riahi, 2004).

## 1.5 De Gennes Blob model for confined polymers

De Gennes modified Flory's model for self-avoiding polymers constrained in a tube of width  $R$  (Daoud et al. 1977, de Gennes, 1979). In the limit that  $R \gg L_p$ , the polymer is free to coil in a channel, since the energy for a molecule to make a backbend is  $\sim k_B T$ . He thus treated the polymer as if it were a series of (named) "blobs", which repel like hard spheres. He treats each blob as a Flory coil. This means that the polymer is evenly distributed along the channel, and (2) the blob radius  $R_F$  scales as  $R$ , the size of the channel, according to Equation 13.

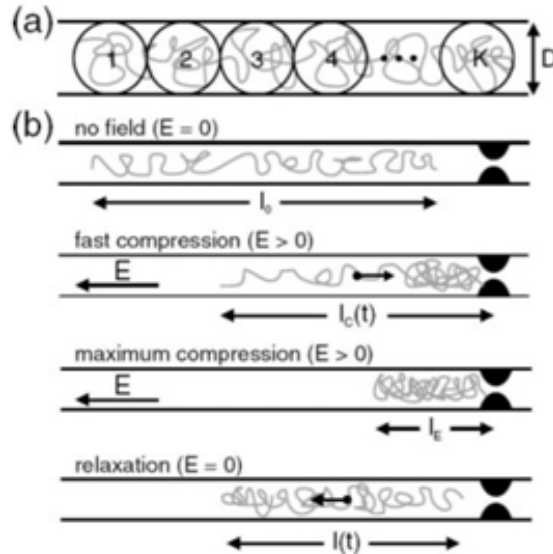


Figure (5)

Fig (5): a) De Gennes' "blob" model of confined DNA in a channel of diameter  $D$  describing the molecule as a series of self avoiding spheres. (b) Experimental stages of compressing a molecule at a constriction (image taken from Mannion and Craighead, 2006).

We are able to find the contour length that is stored in each blob, by back-solving Equation 13 for  $L_B$ , and we find that

$$L_B = \frac{R^{5/3}}{(L_P w_{eff})^{1/3}} \dots\dots\dots(14)$$

The apparent length along the channel  $L_{||}$  is then obtained from

$$L_{||} = R \frac{N}{N_B} = R \frac{L}{L_B} \dots\dots\dots(15)$$

A more rigorous derivation of the extension relationship would minimize the energy of the collection of blobs. For a polymer chain of  $N$  monomers of length  $L_P$ , divided among  $N/N_B$  blobs, we rewrite Equation 10 as

$$F_{total} = k_B T \frac{N}{N_B} \left( \frac{R^2}{l^2 N_B} + \frac{l^2 w_{eff} N_B^2}{R^3} \right) \dots\dots\dots(16)$$

We will consider the apparent length along the axis of the nanochannel as the free parameter, and we find that

$$F_{total} = k_B T \left( \frac{L_{||}^2}{L_P^2 N} + \frac{L_P^2 w_{eff} N^2}{R^2 L_{||}} \right) \dots\dots\dots(17)$$

Taking the derivative of Equation 17 with respect to length  $L_{||}$  and setting it equal to zero, we find the equilibrium length (all factors of order one will be omitted in the following),

$$\frac{\partial F_{total}}{\partial L_{II}} = 0 = k_B T \left( \frac{2L_{II}}{L_p^2 N} - \frac{L_p^2 w_{eff} N^2}{R^2 L_{II}^2} \right) \dots \dots \dots (18)$$

and therefore

$$L_{II} \rightarrow L_o = CL_c \left( \frac{L_p w_{eff}}{R^2} \right)^{1/3} \dots \dots \dots (19)$$

for  $L_c = NL_p$ .  $C$  is a parameter that is common to all systems independent of channel size and polymer. This is in agreement with the more basic argument by De Gennes.

### 1.6 Introduction to micro- and nanochannel devices

Micro- and nano-fluidic devices are a relatively new way of analyzing single molecules and polymers. Devices made from transparent materials enable efficient imaging on the scale of biological interactions, with significantly smaller sample volumes. Nanostructures such as nanoslits, nanopores, and nanochannels have been designed to trap molecules in 1 or 2 spatial dimensions [18]. Channels inside these chips can be produced from microns to a few nanometers in width [18]. The mechanical properties of biological molecules are implicitly related to their function in vivo. Hence, microchannel and nanochannel devices that match the length scales of these interactions are valuable research tools [19].

Nanochannels act to confine bio-molecules by restricting their motion to one dimension along the channel axis. Once driven into the nanochannel, observed molecules are

subject to “confinement induced stretching” in the axial direction because they are compressed in the lateral direction [20]. Molecules that are introduced into micro- and nanochannel chips are directly manipulated by – electro kinetic transport. The stretching of individual molecules for imaging enables sizing of DNA molecules in a few minutes, whereas former gel-based separation techniques would require hours, or even days, to separate genomic length DNA [21, 22].

Instead of the traditional method dealing with ensembles of molecules, it is possible to measure the length of one molecule at a time. In ensemble methods data must be averaged across many molecules, which do not give the properties of single molecules. Stretching inside nanochannels is also an improvement over more traditional single molecules techniques, such as surface stretching methods [23] or adsorbing at the surface of mica [16]. That is because in surface stretching the molecule is locked into a single molecular conformation before measurement of its length. In nanofluidic devices, however, one molecule can be “trapped” within a nanochannel and many independent measurements can be taken while a molecule fluctuates. This allows rapid measurement of genomic DNA with high accuracy, within a few hundred base pairs [21]. Nevertheless, there are some disadvantages to the “lab-on-a-chip” design. Although shearing is avoided in the channels due to the low Reynolds number, very long portions of genomic DNA cannot be pipetted without shearing.

## 1.7 Conformation of molecule in the nano-confinement

We define “confined” as the situation when a polymer is placed in a geometry that has at least one dimension smaller than the polymer’s equilibrium size in a dilute bulk solution  $\sim R_g$ , bulk. In this vein, we define three major types of confinement. Slit-like confinement is defined as when only one dimension of the geometry is smaller than the natural size of a polymer ( $h < R_g$ , bulk). Similarly, tube-like confinement is defined as when a polymer is confined in a tube with a diameter  $h < R_g$ , bulk. In reality, this type of confinement is usually realized as a rectangular channel with its height ( $h$ ) and width ( $d$ ) smaller than  $R_g$ , bulk. Surface confinement is defined as when a polymer is limited to move in a plane. Fig. 6 illustrates these three types of confinement, the relevant theories, and representative fluorescence images of confined  $\lambda$ -DNA. From the fluorescence images in Fig. 6 one can get a feel for the striking conformational changes induced by confinement. Other types of confinements also exist in addition to those mentioned above. For example, it is possible to confine a chain from all three dimensions to form a box-like confinement [24]. A Polymer passing through a point-like pore can be considered as a slip link type confinement [25, 26]. Some studies actually involved these two types of confinements [27], and such combinations are common in many bio-logical processes in cells. Fig.6 illustrates the conformation of DNA molecule in various confinements.



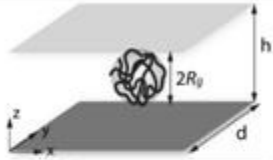
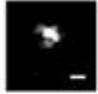


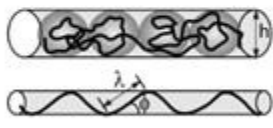



Types of confinement	Models for a confined polymer	Representative images of $\lambda$ -DNA
Bulk or weak confinement	 <p>Flory theory <math>R_g &lt; h, d</math></p>	
Slit-like confinement	 <p>Blob theory <math>p &lt; h &lt; R_g &lt; d</math></p>	
Tube-like confinement	 <p>Blob theory <math>p &lt; h \text{ (and } d) &lt; R_g</math></p> <p>Deflection chain <math>h \text{ (and } d) &lt; p</math></p>	 <p><sup>a</sup></p>
Surface confinement	 <p>Polymer in 2D <math>h \sim 0</math> <math>R_g &lt; d</math></p>	 <p><sup>b</sup></p>

Fig (6): Shows the confinement of DNA in various confinements like weak confinement, slit-like confinement, Tube-like confinement, surface confinement (image taken from Maier and Rädler Phys. Rev. Lett., Copyright 1999 American Physical Society)

## 1.8 References

- [1] Leonard C. Gosule et al Compact form of DNA induced by spermidine. *Nature*, 259, 333-335,(1976).
- [2] Andrew A. Travers DNA Conformation and protein binding. *Annu. Rev. Biochem*, 58:427-52, (1989).
- [3] Francois Luckel et al Enhancement and inhibition of DNA transcriptional activity by spermine: A marked difference between linear and circular templates. *FEBS letters*, 579, 5119-5122 (2005).
- [4] David L. Nelson, Michael M. Cox *Lehninger Principles of Biochemistry*. 4ed W. H.Freeman and Company Press
- [5] U. K. Laemmli Characterization of DNA condensates induced by poly (ethylene oxide) and polylysine. *Proc. Nat. Acad. Sci. USA*, 72, 11, 4288-4292, (1975).
- [6] Malla Kuosmanen et al, Inhibition of the activity of restriction endonuclease by spermidine and spermine. *FEBS*, 179, 17-20, (1985).
- [7] <http://en.wikipedia.org/wiki/Dna>
- [8] [http://en.wikipedia.org/wiki/Worm-like\\_chain](http://en.wikipedia.org/wiki/Worm-like_chain)
- [9] Claudio Rivetti et al, Scanning force microscopy of DNA deposited onto mica: equilibration versus kinetic trapping studied by statistical polymer chain analysis. *J. Mol. Biol.*, 264, 919-932, (1996).
- [10] Dale Kaiser et al, DNA packaging steps in bacteriophage Lambda head assembly. *J. Mol. Biol.*, 91, 175-186, (1975).
- [11] Sonia Cunha et al, Isolation of the *Escherichia coli* nucleoid. *Biochimie*, 83, 149-154. (2001).
- [12] T. Thomas et al, Polyamines in cell growth and cell death: molecular mechanisms and therapeutic applications. *CMLS*, 58, 244-258,67, (2001).
- [13] Amin Ahmed Ouameur et al Structural analysis of DNA interactions with biogenic polyamines and cobalt (III) hexamine studied by Fourier transform infrared and capillary electrophoresis. *The journal of Biological Chemistry*,279, 40, 42041-42054, (2004).

[14] <http://en.wikipedia.org/wiki/Spermidine>

[15] Isabel Baeza et al Electron microscopy and biochemical properties of polyamine-compacted DNA. *Biochemistry*, 26, 6387-6392, (1987).

[16] Zhang Lin et al, The observation of the local ordering characteristics of spermidine condensed DNA: atomic force microscopy and polarizing microscopy studies. *Nucleic acids research*, 26, 13, 3228-3234, (1998).

[17] Ye Fang et al, Early intermediates in spermidine-induced DNA Condensation on the surface of mica. *Am. Chem. Soc.*, 120, 35, (1998).

[18] Robert Riehn et al, "Nanochannels for Genomic DNA Analysis: The long and short of it." *Integrated Biochips for DNA analysis*. Eds. R.H. Liu and A.P. Lee. Landes Bioscience, Austin, Texas. 151-186, (2007).

[19] Meyers, R.A. *Molecular Biology and Biotechnology: a comprehensive desk reference*. New York: Wiley- VCH, 1995.

[20] Tegenfeldt, J.O. et al, "The dynamics of genomic-length DNA molecules in 100 nm channels," *Proc. Natl. Acad. Sci. USA*, 101, 10979-10983, (2004).

[21] Cox, E.C. et al, "Electrophoretic karyotype for *Dictyostelium discoideum*," *Proc. Natl. Acad. Sci. USA*, 87, 8247-8251.(1990).

[22] Huang, Z. et al, "Large DNA fragment sizing by flow cytometry: application to the characterization of P1 artificial chromosome (PAC) clones," *Nucl. Acids Res.*, 24(2), 4202-4209. (1996).

[23] Bensimon, D. et al, "Stretching DNA with a Receding Meniscus: Experiments and Models," *Physical Review Letters*, 74(23), (1995).

[24] Sakaue, T. et al, Polymer chains in confined spaces and flow-injection problems: Some remarks, *Macromolecules* 39, 2621-2628, (2006).

[25] Kasianowicz et al, Characterization of individual polynucleotide molecules using a membrane channel, *Proc. Natl. Acad. Sci. USA* 93, 13770-13773,(1996).

[26] Lubensky et al, 1999, Driven polymer translocation through a narrow pore, *Biophys. J.* 77, 1824-1838.

[27] Nykypanchuk et al, Brownian motion of DNA confined within a two dimensional array, *Science* 297, 987-990. (2002)

## **Chapter 2 Materials and methods**

### **2.1 Introduction to YOYO-1 and DAPI**

The stable fluorescence nucleic acid dye, YOYO-1 (molecular weight: 1270.65 Dalton) (Invitrogen, CA) is found to bis-intercalate into the base pair of the dsDNA by electrostatic interactions. The excitation wavelength of YOYO-1 intercalated DNA is 491nm and the emission wavelength is 509nm. The reason behind using YOYO-1 is its high fluorescence intensity and low back ground noise. However by using YOYO-1 several properties of the DNA such as persistence length and contour length of the DNA get increased where as the charge of the DNA molecule get decreased [1, 2, 7]. On the other hand the minor groove binding fluorescence labeling dye 49, 6-diamidino-2-phenylindole (DAPI, excitation wavelength 358nm, emission wavelength 461nm) (Invitrogen, CA) which show less effect on the contour length and persistence length of DNA molecule when compared to YOYO-1.

### **2.2 DNA sample preparation**

DNA stock solution is prepared in 1XT buffer(10mM Tris-Hcl) pH=8.5 at a concentration of 0.02g/l. YOYO-1 stock solution is prepared in 1XT buffer pH=8.5 at a concentration of 5 $\mu$ M. In our experiments, the ratio of DNA base pair to YOYO-1 molecule is fixed at 23 to 1 (base pairs: YOYO-1). After adding YOYO-1 the solution is incubated at room temperature for 1hr to have uniform distribution of the YOYO-1 on the DNA molecule. The DNA-YOYO mixture is diluted to a final concentration of 0.1 $\mu$ M in base pairs with 1XT, condensing ligand buffer. The solution is incubated for 3hrs to achieve equilibrium.

Note that the length of the incubation time with condensing ligands will affect the equilibrium conformation of the DNA molecule. During the incubation time the solutions are protected from light to avoid photo bleaching and photo damage of the DNA molecules. After the incubation the 3-5 $\mu$ l of the solution is placed on the cover slip or the sample cell to do fluorescence experiments.

The single molecules were identified from the intensity profile of molecules [2, 3]. The intensity of the condensed DNA molecule will be very high when compared to the intensity of the coiled state DNA molecule. The aggregates or broken pieces of the DNA molecule were not considered. Long axis distance of the molecule is measured for the coiled and globule states of the DNA molecule. We observe the fluorescence of the dye which is attached to the DNA molecules. The coil is characterized by the internal fluctuation and translational Brownian motion of the DNA molecule. The DNA molecule in the elongated state is shown below Fig. (7a). The globule state is characterized by the bright spot exhibiting Brownian motion. The globule state of the DNA molecule is shown in the Fig. (7b). At a critical concentration of the condensing ligand the transition from the coil state to the condensed state takes place. Around the critical concentration of the condensing ligands co-existence of the coil and globule states are observed, in agreement with a first order transition.

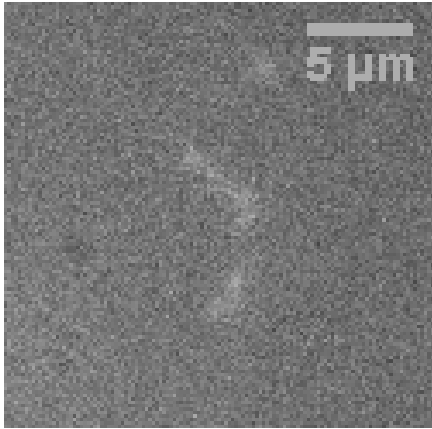


Fig (7a)

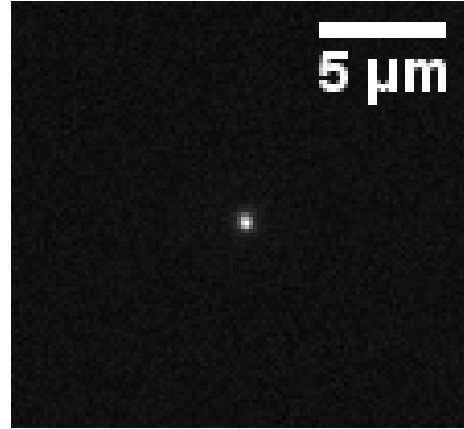


Fig (7b)

Fig (7a): shows the coiled state of the DNA molecule, Fig (7b): shows the condensed form of the DNA molecule

### **2.3 Fabrication of micro and nano-channels**

The stamp was fabricated by a two step lithography process. The nano-channels were fabricated by proton beam lithography in Hydrogen Silsequioxane resist (HSQ) (Dow corning) [4, 5, and 6]. The micro-channels were fabricated by alignment UV-Lithography in SU-8 2005(Micro chem.). Both lithography steps are illustrated below.

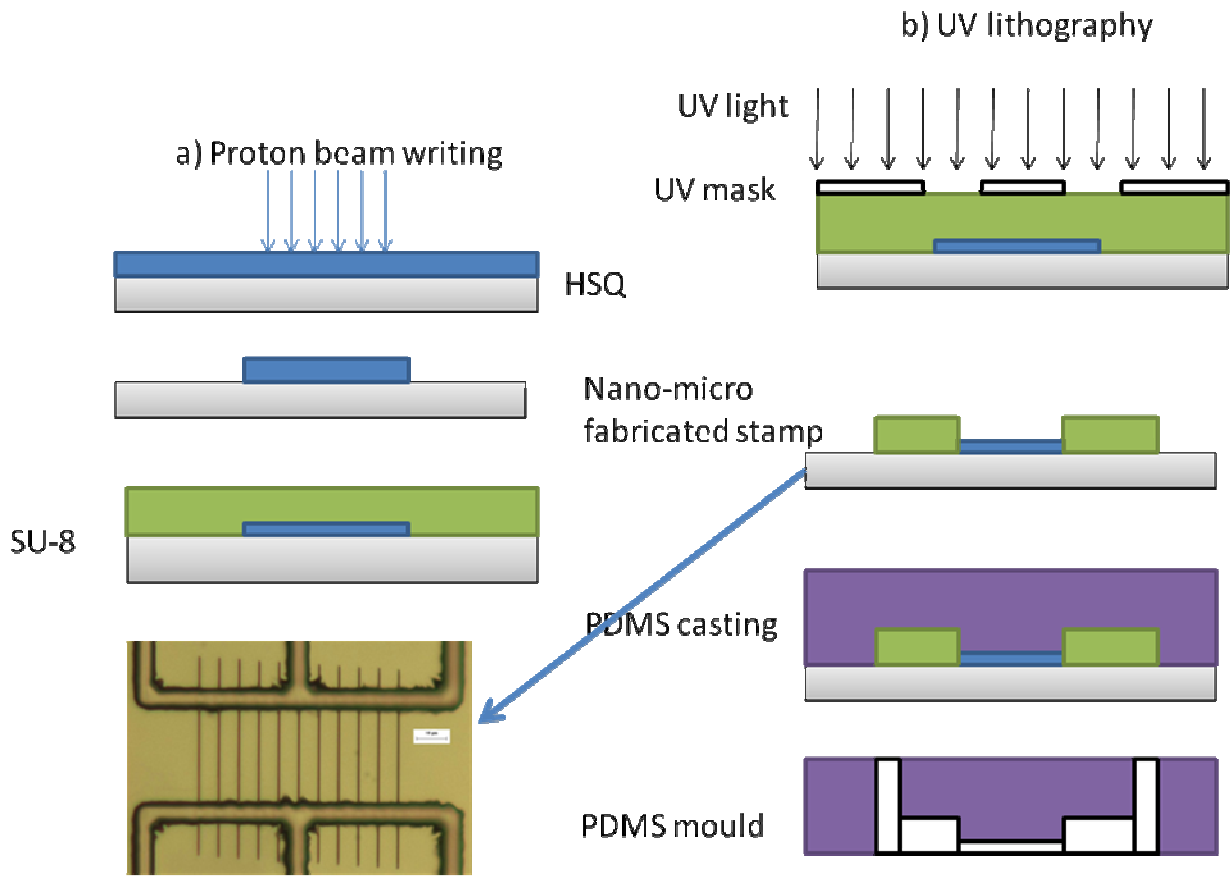


Fig (8): Schematic illustration of the fabrication process of the micro- and nano-fluidic device. (a) Nanostructure patterning in HSQ photo resist by PBW. (b) Super positioning of the SU8 microstructure on the HSQ nanostructure by UV lithography [4-7].

## 2.4 Fabrication of micro channels

SU-8 2005 Photo resist is spin coated on a silicon substrate with suitable spin coating parameters to produce 5 $\mu$ m thick film of SU-8.

- The substrate needs to be preheated on a hot plate at 200 $^{\circ}$ C for 15min.
- The SU-8 is subsequently spin-coated on the substrate at 3000 rpm for 30 s.
- The SU-8 coated substrate is then pre-baked on a hot plate at 65 $^{\circ}$ C for 2 min in order to evaporate the solvent.
- The SU-8 coated substrate is then soft-baked on a hot plate at 95 $^{\circ}$ C for 4 min in order to evaporate the solvent
- The nanostructure on the substrate is aligned with the microstructure on the UV mask with an UV mask aligner system. The substrate is exposed to UV light (365 nm) for 4min.
- Post-bake 1: The exposed substrate is baked at 65 $^{\circ}$ C for 2min.
- Post-bake 2: The exposed substrate is baked at 95 $^{\circ}$ C for 2min.
- Structures are developed by immersion in SU-8 developer (MicroChem $_{TM}$ ) for 120 s, followed by a brief rinse with IPA, then a rinse with deionized water, and eventually drying with a gentle stream of dry nitrogen gas.
- Now the stamp containing nano and micro structures is further baked at 150 $^{\circ}$ C for 30 min to further harden the resist.

## 2.5 Fabrication of nano-channels

- Coat a metal layer on silicon for easy release of PDMS.
- Spin coat HSQ
- Bake the wafer at 150 $^{\circ}$ C for 2min



- Proton beam writing
- Development in 2.38% TMAH for 60 sec
- DI water rinse

## **2.5 Transfer of nano-micro structures to PDMS**

The nano and micro structures are transferred into Polydimethylsiloxane (PDMS) (Dow corning). The curing agent (Dow corning) is mixed to the PDMS in the ratio of 1:10. The mixture is degassed for 30min to remove air bubbles. Now the mixture is poured on to the stamp and kept in the oven at 65°C for 6hrs. Once the PDMS is hardened the PDMS is peeled off the stamp very gently [7]. The separated PDMS contains nano and micro structures. The reservoirs are made with punchers (Ted Pella) of diameter 1.5mm.

## **2.6 Air plasma treatment**

The bonding between PDMS and the cover slip is greatly enhanced by plasma treatment of PDMS and cover slip. The bonding between PDMS and coverslip plays a crucial role in micro and nano-channel devices. The pressure exerted on the fluid inside the device is very high and is inversely proportional to the cross section of the channels. Therefore with proper sealing leakage of the fluid can be avoided. The oxidized PDMS surface contains negative charged surface groups which resist the adsorption of the DNA molecules. After plasma treatment the PDMS is hydrophilic for 45 min in air [9]. After this time the hydrophobicity of the PDMS is recovered. Once the PDMS is peeled from the master stamp holes of diameter 1.5mm were punched at the end of the micro

channel with punchers (Ted Pella). The PDMS is cut into slabs of length 1cm, breadth 1cm and thickness of 0.2cm to 0.3cm. The PDMS strip and the cover slip are placed in a cylindrical type glow discharge cell. The air plasma treatment is done in medium power mode at radio frequency of 40 KHz. The PDMS and cover slip are air plasma treated for 30s at a pressure of 0.3 Torr [7]. Once the plasma treatment is finished, PDMS is immediately kept on coverslip and baked at 65°C for 1min to further improve the adhesion of PDMS to the cover slip. Fig. (9) shows the nano-micro fluidic chip.

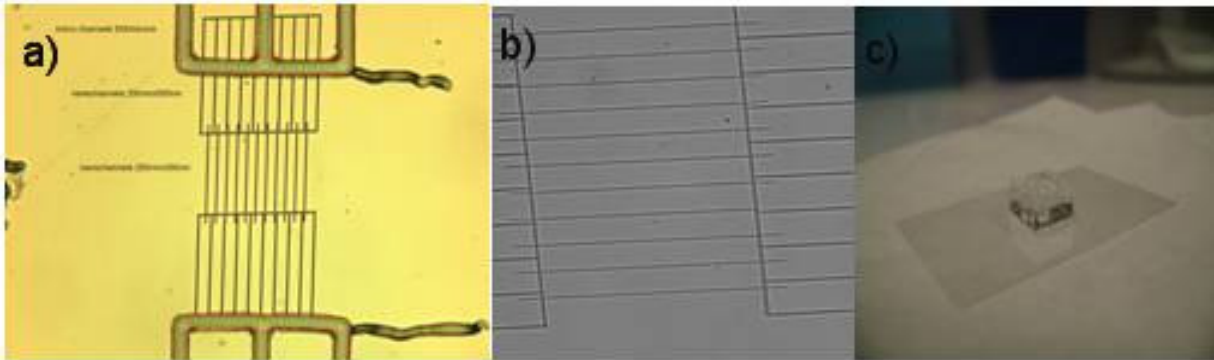


Fig (9): a) shows the nano-channels of dimensions 200nmX300nm on silicon substrate b)shows the channels in PDMS chip after bonding to the cover slip. c) Shows the picture of nano-micro fluidic ship.

## 2.7 Injecting molecules into nano-channels

T4(165,600 bp; Nippon Gene) DNA molecules of concentration (1 $\mu$ M of bp) were prepared in various buffers like 1XT (10mM Tris-Hcl, pH=8.5), 1XTBE,pH=8.5 (90mM Tris,90mM Boric acid,2mM EDTA). The molecules were intercalated with YOYO-1(Invitrogen, Carlsbad, CA) Dye at ratio of 1:23. The molecules are loaded into reservoirs. Due to capillary action the molecules diffuse to the nano-channels. DNA was visualized with inverted epi-fluorescence microscope (Olympus iX71) equipped with EM mode camera (Photo metrics). Two platinum wires were inserted into the reservoirs and connected to the power supply (keithley 237). The motion of the molecules can be controlled by the electric field [8]. The buffer system can affect the motion of the molecules. In 1XT buffer (low ionic strength) electro-osmosis (negative charged molecule moves towards negative electrode) takes place. In 5XTBE buffer (high ionic strength) electrophoresis (negative charged molecule moves towards positive electrode) takes place. The movies were collected at a frame rate of 33fps.

## **2.8 Florescence imaging of T4 DNA molecules in nano-channels**

The YOYO-1 stained DNA molecules were prepared in relevant buffer conditions and loaded into the reservoirs connected to the micro channels. The DNA molecules were driven in the nano-channels by applying electric field. Two electrodes were immersed in the two reservoirs and molecules were driven into the nano-channels either by electrophoresis or electro-osmosis. Once the DNA molecules were driven into nano-channels the field is switched off for 1-2min for the molecules to arrive at equilibrium configuration [7]. The fluorescence of the stained DNA molecules was imaged using a 100X oil immersion objective. The exposure time of the excitation light was controlled by a UV light shutter and attenuators. The extension of the observed DNA molecules was measured by imageJ (<http://rsb.info.nih.gov/ij>).

## 2.11 References

- [1] Natsuhiko Yoshinaga et al, Intercalating Fluorescence Dye YOYO-1 Prevents the Folding Transition in Giant Duplex DNA, *Biochemical and Biophysical Research Communications* 286, 264–267 (2001).
- [2] K. Yoshikawa et al, Large Discrete Transition in a Single DNA Molecule Appears Continuous in the Ensemble, *Phys. Rev. Lett.* 76, 3029, (1996).
- [3] M. Takahashi et al, Discrete Coil-Globule Transition of Single Duplex DNAs Induced by Polyamines, *J. Phys. Chem. B* 1997, 101, 9396-9401
- [4] P.G. Shao et al, Poly (dimethyl siloxane), micro/nanostructure replication using proton beam written masters, *Nuclear Instruments and Methods in Physics Research B* 260 (2007).
- [5] Jeroen A. van Kan et al, Proton Beam Writing of 3D Nanostructures in Hydrogen Silsesquioxane, *Nano Letters* 6, 579-582, (2006).
- [6] J. A. van Kan et al, Three dimensional nanolithography using proton beam writing, *Applied Physics Letters* 83, 1629-1631, 1629, (2003).
- [7] Ce Zhang et al, Effects of electrostatic screening on the conformation of single DNA molecules confined in a nanochannel, *The Journal of Chemical Physics* 128, 225109, (2008).
- [8] L. C. Campbell et al, Electrophoretic manipulation of single DNA molecules in nanofabricated capillaries, *Lab Chip*, 4, 225 – 229, (2004).
- [9] Dhananjay Bodas, Chantal Khan-Malek, Hydrophilization and hydrophobic recovery of PDMS by oxygen plasma and chemical treatment—An SEM investigation, *Sensors and Actuators B* 123,368–373, (2007).

## Chapter 3 Effect of polyamines on the conformation DNA

**3.1 Abstract** In this chapter our main interest is to study the conformation of T4 DNA molecule in the presence multivalent cations like spermidine, cobalthexamine and spermine. To observe the conformation of dye labeled T4 DNA molecule we used fluorescence microscope. Our results show that transition from elongated state to collapsed state is discrete. The critical concentration of the cation needed to condense the DNA molecule is lowest for the tetravalent cation and highest for the trivalent cation. The co-existence region is larger for trivalent cation and less for the tetravalent cation

### 3.2 Introduction

In biological systems, DNAs on the order of  $10^2$ - $10^4$   $\mu\text{m}$  long are usually packed in a narrow space on the order of only 0.1-1  $\mu\text{m}$ , i.e., bacteriophage head, cytoplasmic space in prokaryote, and nucleus in eukaryote [1].

On the other hand, DNA chains exhibit a highly elongated coiled state in aqueous solution in the absence of condensation agents. Thus, the study of the collapsed and decollapsed transition of long duplex DNAs [2-8] is expected to shed light on the dynamic change in the state of DNAs in a living cellular environment. Various chemical species, such as histone proteins, metal cations, and polyamines, are known to induce the compaction of long DNA chains. Polyamines are widespread in both prokaryote and eukaryotes cells and possess various biological effects. For example, it is known that  $\lambda$ -

phage is not generated in polyamine-required mutant *E. coli*. [9] In eukaryote cells, polyamines play an essential role in the growth tissues [10,11].

Several experimental studies have examined the interplay between polyamines and DNA [12-17]. Theoretical investigations have also been performed following by the development of the theory on polyelectrolytes [18-20] and polymers in general [21-24]. However, it has been difficult to obtain fully conclusive results from experiments on the physicochemical properties of the coil globule transition in single DNA chains, since competition is always present between single-chain events and the aggregation of a number of chains under usual experimental conditions. Actually, single-chain observation in aqueous solutions, in its strict sense, has been impossible with conventional experimental methods such as light scattering, X-ray analysis, and sedimentation. These methods require a relatively high concentration (more than about several  $\mu\text{g/mL}$  or  $10 \mu\text{M}$  in base pair (concentration) to obtain adequate sensitivity. In addition, these experimental methods provide information essential only to the characteristics of the ensemble of polymer chains in solution.

Fluorescence microscopy is useful for observing single molecules of long duplex DNA chains. It is reported that individual DNA molecules undergo a first-order transition between an elongated coil state and a compacted globule state with the addition of various kinds of condensing agents, such as neutral flexible polymer [25] cationic and neutral surfactants [26] alcohol [27] polyamine spermidine [28] and inorganic metal cation [29].

We observed changes in the structure of T4DNA by fluorescence microscopy upon the addition of polyamines with different valences: spermine (SPM) with four positive charges, cobalt hexammine with three charges and spermidine (SPD) with three positive charges. We have studied the fragmentation of the T4 DNA molecules upon incidence of light in the presence of condensing ligands and in the absence of condensing ligands.

### 3.3 Fragmentation of the DNA molecules with incident light

Fig. (10) shows the fragmentation of the YOYO-1 intercalated DNA molecule when the molecules are illuminated with light of wavelength 491nm. The photo damage to the DNA molecule can be reduced by lowering the intensity of the light, by adding  $\beta$ -mercaptoethanol, and lowering the concentration of YOYO-1 [30]. Similar results were obtained when DAPI was used. The photo damage to the DNA molecule increases in the presence of condensing ligands. As the charge of the condensing ligand increases the photo damage to the DNA molecule increases. Fig.11 shows the fluorescence damage of the DNA molecule in the presence of 400 $\mu$ M Spermidine.

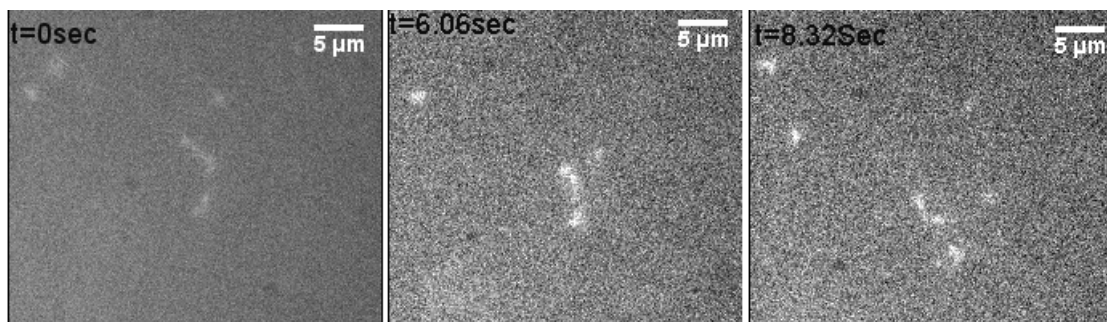




Figure (10): Time sequence of a molecule of T4 as it is labeled with YOYO-1 as it explodes in several short fragments upon intense illumination.

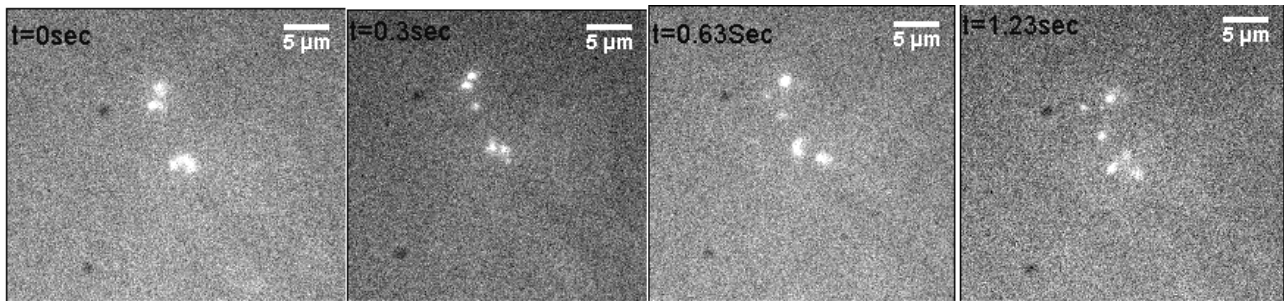


Figure (11): Time sequence of a molecule of T4 as it is labeled with YOYO-1 as it explodes in several short fragments upon intense illumination. The sample contains 400μM Spermidine.

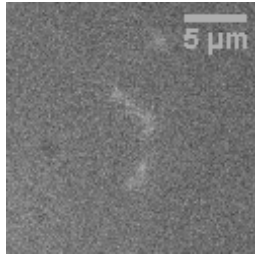
### 3.4 Condensation of DNA observed with fluorescence microscope

In chapter 1, we had introduced the biological meaning and the effect of spermidine on DNA. The conformation and the flexibility of DNA will be changed in the presence of polyamines. In our study, we investigate the polyamine induced condensation of DNA. There are three phases observed with respect to the concentration of polyamines 1) coil 2) coil and globule, and 3) globule. Fig.12 shows the Brownian motion of the DNA molecule in coiled state.



Figure (12): Brownian motion of the DNA molecule

13a) Coiled state



13b) Globule state

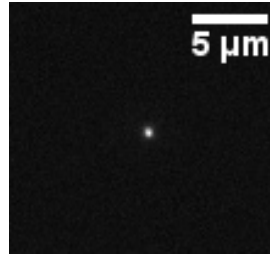


Fig (13a): shows the coiled state of the DNA molecule, Fig (13b): shows the condensed form of the DNA molecule

### **3.5 The conformation of DNA in the presence of polyamines:**

#### **3.5.1 Folding transition of T4 DNA in the presence of spermidine**

Different states of DNA molecules in the presence of spermidine are observed with the fluorescence microscope and recorded in avi format at a frame rate of 33fps. These DNA-SPD complex samples are obtained by gradually increasing the concentrations of spermidine. As the spermidine concentration is increased the DNA molecule switched from the coil state to the condensed state [28, 43, 45]. In the lower concentration of spermidine the molecules are coil and at the higher concentration of spermidine the molecules are globule. Around the transition point the coexistence of the both coil and condensed states are observed; this is known as the co-existence region of both states [28, 43, 45]. The DNA molecules in the coil form have less intensity where as in the condensed state the molecules have very high intensity [23, 43, 45]. Fig.14 shows the histogram of the long axis distance of the T4 DNA molecules. Long axis distance is the longest distance within the fluorescence image of the DNA chain in a two dimensional plane. Fig.14 shows the long axis distance of the DNA molecules with various concentration of spermidine. The spermidine concentration is varied from 0μM to 1mM.

At lower concentration from 0 $\mu$ M to 400 $\mu$ M coil state of the DNA molecules exists. From 500 $\mu$ M- 600 $\mu$ M co-existence of the coils and globules exists. Above 750 $\mu$ M condensed state of the DNA molecule exists. The concentration of DNA is 0.1 $\mu$ M in base pairs. Binding ratio of the YOYO to the base pair is 1:23. The buffer system used is 1XT (10mM tris, pH=8.5). Fig.14 shows the histogram of the long axis distance of the DNA molecules at concentrations 40 $\mu$ M, 400 $\mu$ M, 500 $\mu$ M, 600 $\mu$ M, 750 $\mu$ M and 800 $\mu$ M of spermidine. By using mat lab code, the movies are analyzed frame by frame to deduce the long axis distance of the DNA molecules.

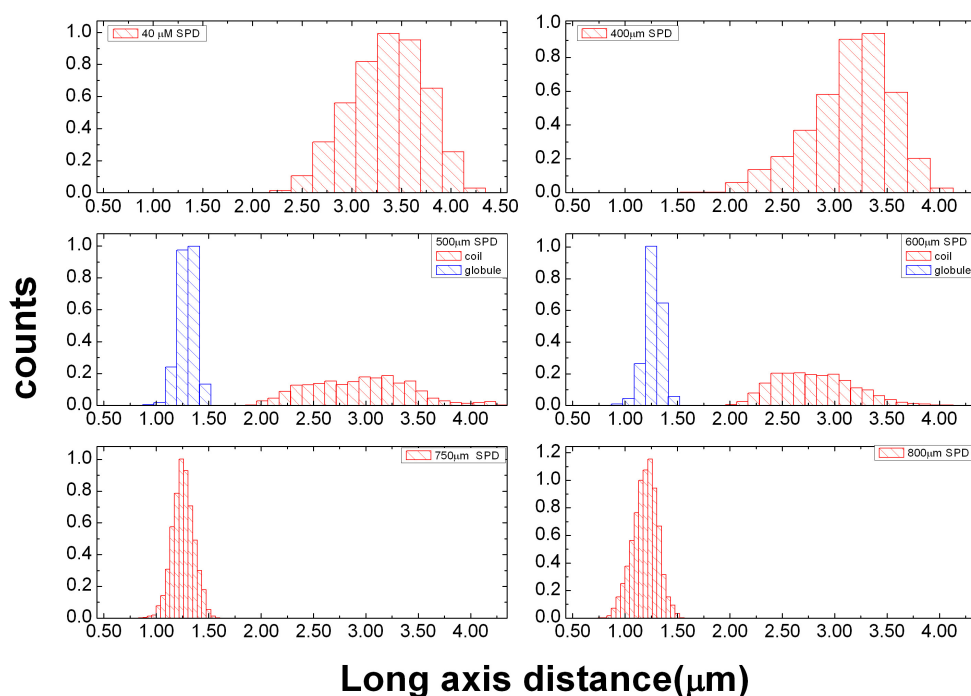


Figure (14): Histograms showing the distribution of the conformation of the DNA molecules with various concentrations of the spermidine

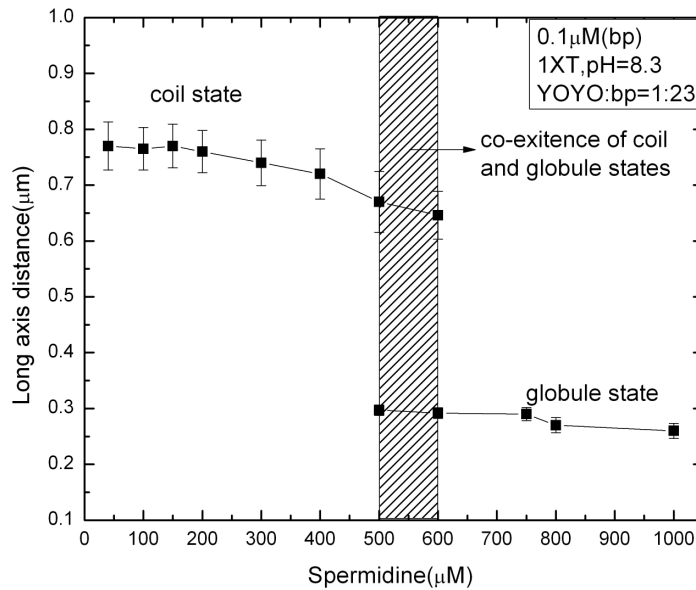


Figure (15): Phase diagram showing the different states of the DNA molecule with increasing concentration of the spermidine.

### 3.5.2 Conformation of DNA in the presence of cobalt hexamine tri chloride (CoHex)

The movies of different states of DNA in the presence of cobalt hexamine tri chloride (CoHex) are observed with the fluorescence microscope. These DNA-CoHex complex samples are obtained by gradually increasing the concentrations of CoHex. As the CoHex concentration is increased the DNA molecule switched from the coil state to the condensed state. In the lower concentration of CoHex the molecules are coiled and at the higher concentration of CoHex the molecules are condensed. Around the transition point the coexistence of both coil and condensed states are observed. When compared to spermidine at very low concentration of CoHex around 100μM the compaction of DNA is observed [17, 44]. This can be explained by the higher binding constant of CoHex to the DNA than SPD. The photo damage to the DNA molecule in the presence of CoHex is more when compared to SPD.

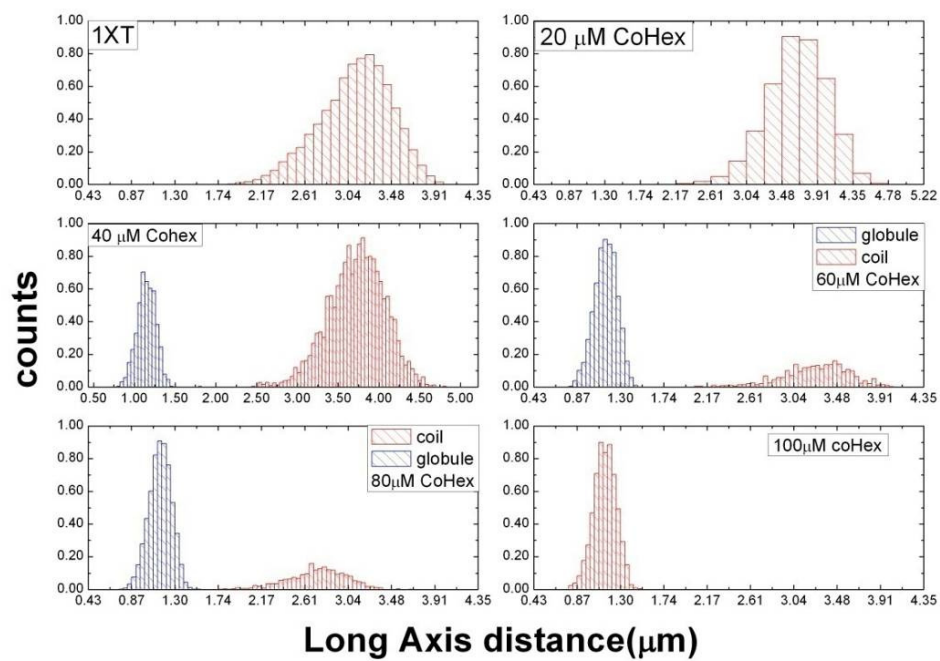


Fig (16): Histograms showing the distribution of the conformation of the DNA molecules with various concentrations of the CoHex

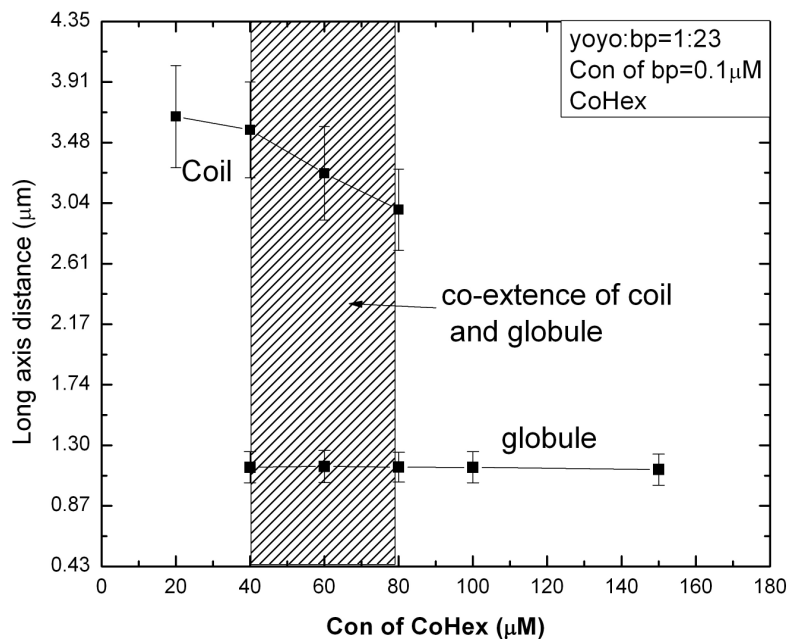


Figure (17): Phase diagram showing the different states of the DNA molecule with increasing concentration of the CoHex

### **3.5.3 Conformation of DNA in the presence of spermine tetra chloride (SPE)**

The movies of different states of DNA in the presence of spermine tetra chloride (SPE) are observed with the fluorescence microscope. These DNA-SPE complex samples are obtained by gradually increasing the concentrations of SPE. As the SPE concentration is increased the DNA molecule switches from the coil state to the condensed state. For lower concentrations of SPE the molecules are coiled; and for higher concentrations of SPE, the molecules are condensed. Around the transition point, the coexistence of the both coil and condensed states (co-existence region) are observed [28, 43, 45]. When compared to spermidine and CoHex at very low concentration of SPE around 6 $\mu$ M the compaction of DNA is observed. This can be explained by the higher binding constant of SPE to the DNA than SPD and greater charge of SPE than SPD and CoHex. The photo damage to the DNA molecule in the presence of SPE is greater when compared to the SPD and CoHex.

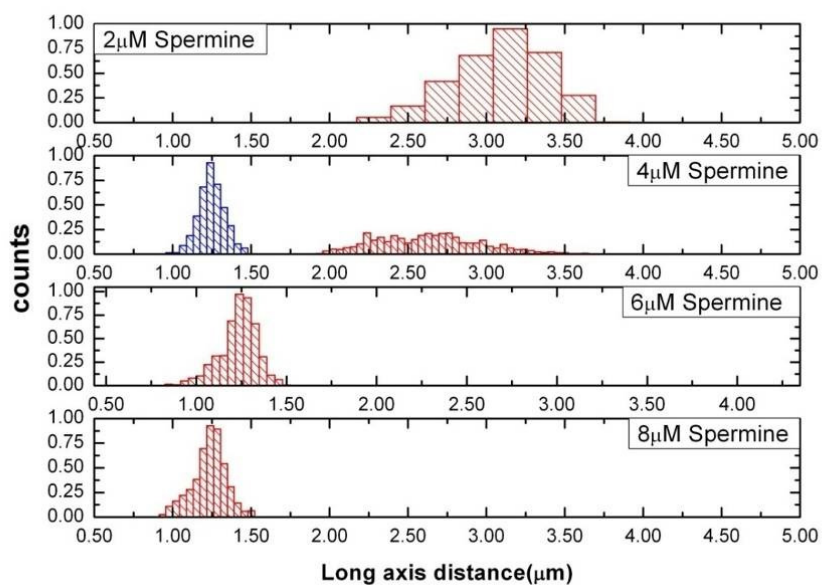


Fig (18a): Histograms showing the distribution of the conformation of the DNA molecules with various concentrations of the SPE

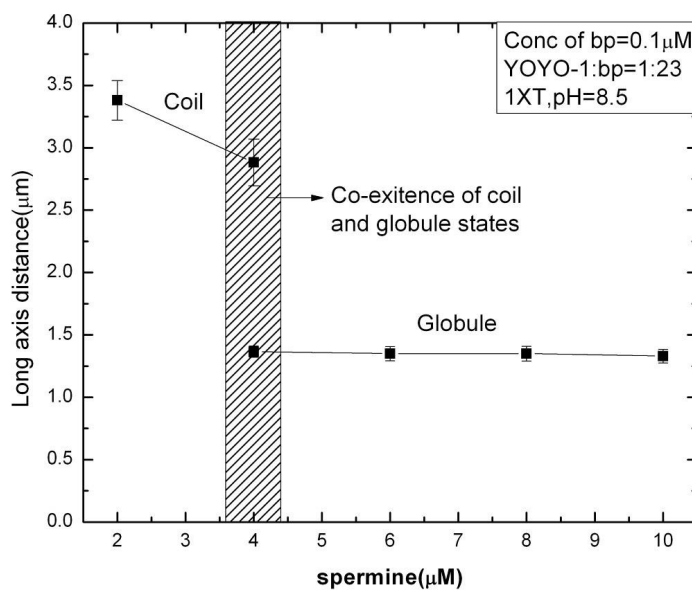


Fig (18b): Phase diagram showing the different states of the DNA molecule with increasing concentration of the CoHex

### **3.6 Effect of fluorescence dye on the conformation of DNA molecule**

There have been significant advances in the methods of observing individual molecules in recent years. Single molecular observation can provide direct information on the structure and function of individual molecules. Among the methods for single molecule observation, fluorescence microscopy has shown to be very useful to image time trajectories of the shape of individual giant DNA molecules [31–34]. It has been found that a single giant duplex DNA undergoes a large discrete transition from an elongated coil state to a folded compact state, with the addition of various kinds of condensing agents by distinguishing intramolecular collapse [35–37] from inter-molecular condensation of DNAs (38 –40). To visualize DNA, it must be stained with suitable fluorescence dyes. Among dyes, an intercalator, YOYO-1, is often used for direct observation of DNA because it provides high fluorescence intensity specific to DNA and a low background [41, 42]. On the other hand, it has been reported that DAPI exhibits a smaller effect on the DNA conformation, on contour and persistence lengths, than intercalators do. In the present study, we evaluated the effects of DAPI and YOYO-1 on the folding transition of giant DNAs induced by spermidine, with fluorescence microscopy. Our results indicate that with DAPI the compaction of the DNA molecule takes place at lower concentration of Spermidine when compared to YOYO-1[43]. DAPI attaches only to the minor groove of DNA. The excitation wavelength is 350nm and the emission wavelength is 461nm (blue color). Fig. 19 shows the distribution of the long axis distance of the DNA molecules with various concentrations of the spermidine. Fig.20 shows the phase diagram of the states of the DNA molecule intercalated with DAPI with increasing concentration of spermidine.



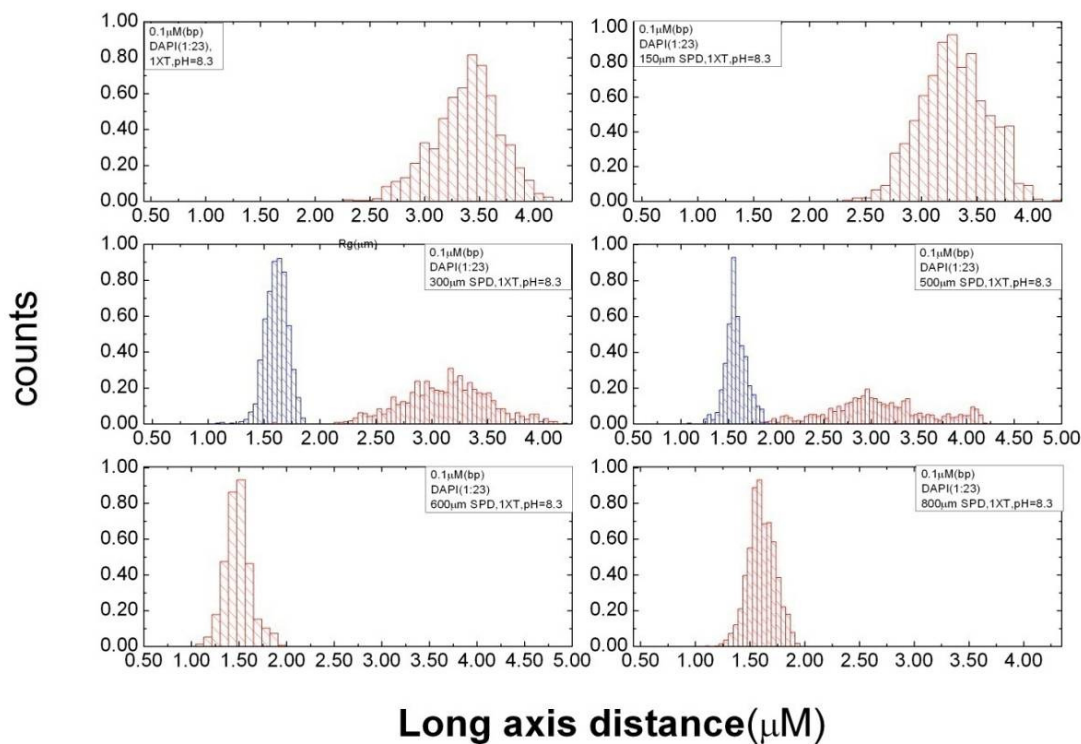


Fig (19): Histograms showing the distribution of the conformation of the DAPI- DNA molecules with various concentrations of the spermidine

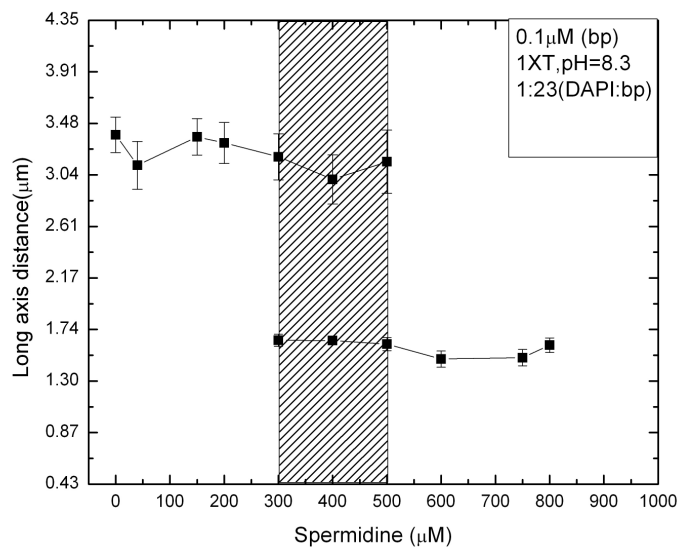


Figure (20): Phase diagram showing the different states of the DAPI-DNA molecule with increasing concentration of the spermidine.

From Fig (15) in the case of YOYO-1 intercalated DNA molecules the critical concentration of spermidine needed to condense the DNA molecules is  $750\mu\text{M}$ . From Fig (20) in the case of DAPI labeled DNA molecules the critical concentration of spermidine needed to condense the DNA molecules is  $600\mu\text{M}$ . It is known that intercalators elongate the coiled duplex DNA chain and increase the stiffness of the DNA chain [43]. An increase in the stiffness in the duplex DNA should cause instability in the compacted state. Because of the instability in the compacted state, it is expected that DNA molecules to be in elongated coil state. Consequently the phenomena we observed here with YOYO-1 would be common to most other intercalators and give us interaction of intercalators with higher order of structure of DNA.

### 3.7 DNA concentration effects

Condensation by spermidine has been studied for different concentrations of base pairs ranging from  $0.1\mu\text{M}$  to  $5\mu\text{M}$ . In these experiments 1XT pH=8.5 buffer is used. In all these experiments the binding ratio between YOYO-1 and base pairs is fixed at 1:23. Fig. 21b shows the phase-diagrams for concentration of base pairs (bp):  $0.1\mu\text{M}$ ,  $1\mu\text{M}$ ,  $5\mu\text{M}$ . Above  $1\mu\text{M}$  concentration of bp, aggregation of the molecules cannot be disregarded in the presence of spermidine, therefore we have observed only elongated molecules (may not be single) and globules. Fig. (21a) shows the fluorescence microscope images of T4 DNA molecules stained by the fluorescent dye YOYO-1. At low concentration of DNA molecules [bp] =  $0.1\mu\text{M}$ , individual DNA molecules undergo large discrete transition from an elongated coil state to folded compact state with an increase in the concentration of condensing agent. At low concentration of DNA molecules the phase transition occurs at  $750\mu\text{M}$  concentration of spermidine. At high concentration of DNA molecules [bp]= $5\mu\text{M}$  the same phase transition is observed under the spermidine concentration similar to that used to induce the folding transition from coiled to compact states in the diluted DNA solution[48]. At high concentration of DNA molecules the phase transition occurs at  $800\mu\text{M}$  concentration of spermidine Therefore critical concentration of spermidine needed for the phase transition remains constant irrespective of the concentration of the base pairs, indicating that this can be an intrinsic variable that depends on the polyamine [48].

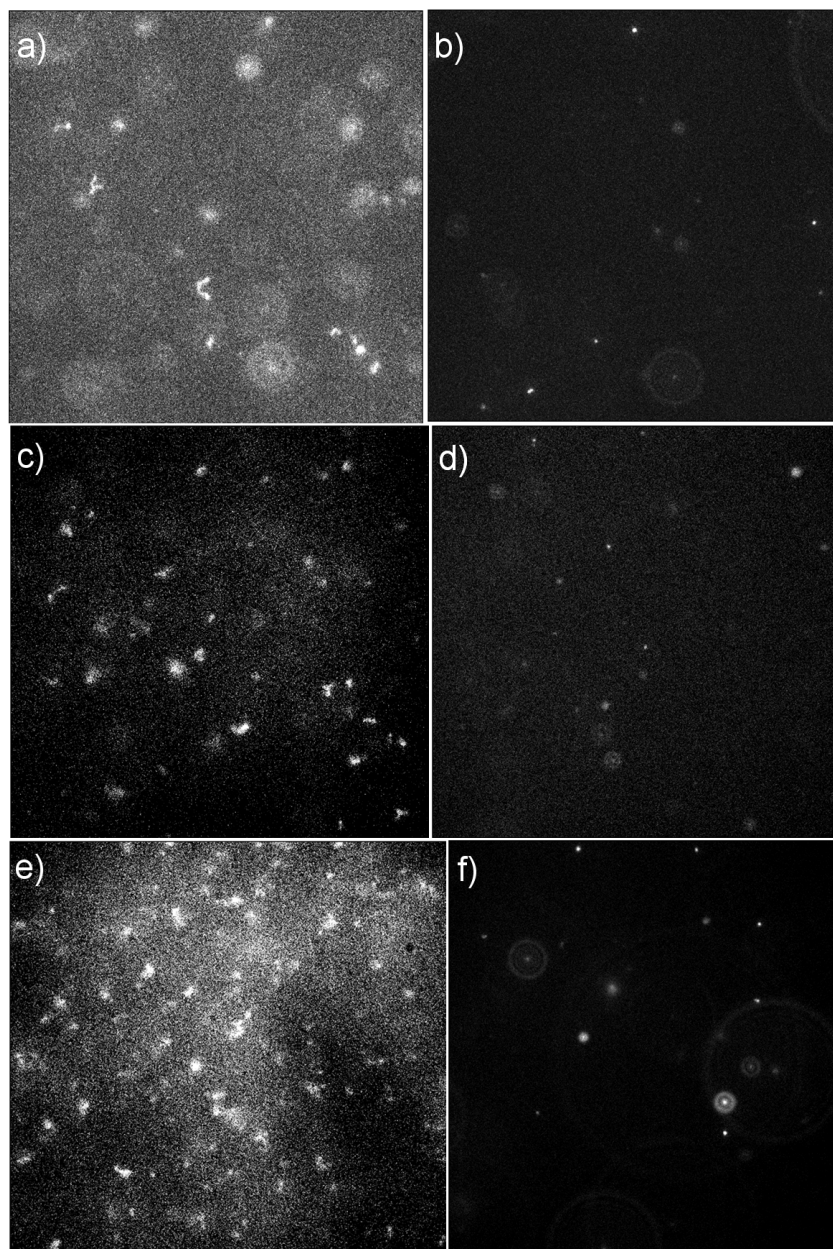


Fig: (21a) shows the fluorescence image of T4 DNA at various DNA concentrations. a) conc of bp=0.1 $\mu$ M and [SPD]=0 $\mu$ M b) conc of bp=0.1 $\mu$ M and [SPD]=750 $\mu$ M c) conc of bp=1 $\mu$ M and [SPD]=0 $\mu$ M d) conc of bp= 1 $\mu$ M and [SPD]=750 $\mu$ M e) conc of bp=5 $\mu$ M and [SPD]=0 $\mu$ M f) conc of bp=5 $\mu$ M and [SPD]=800 $\mu$ M

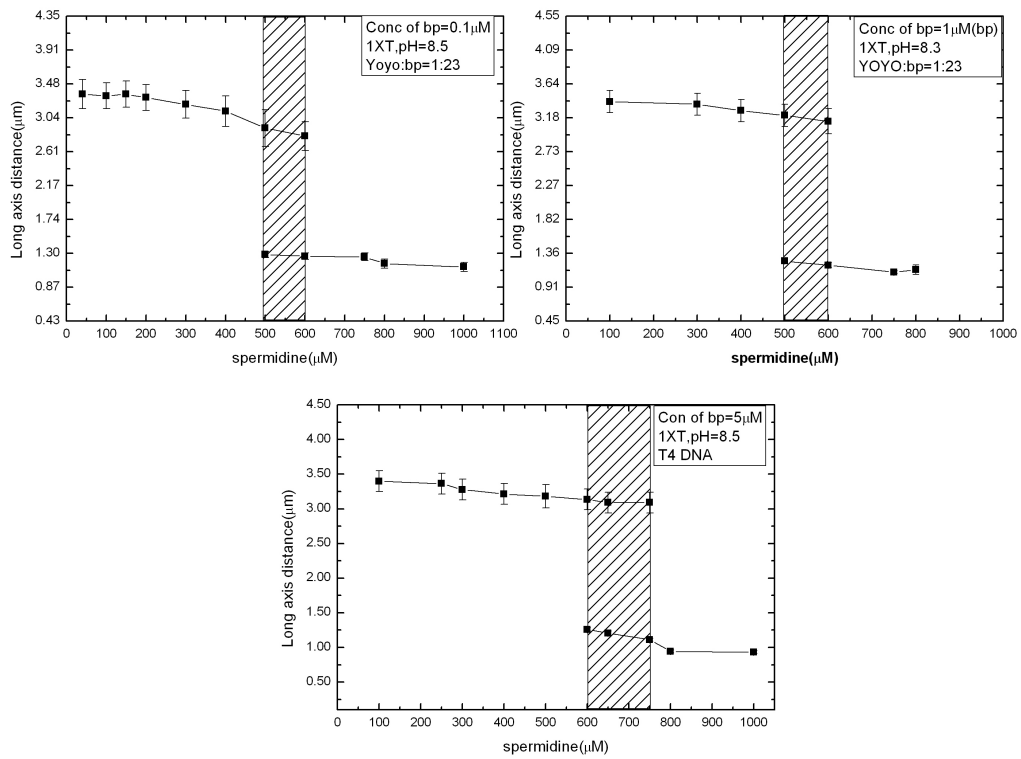


Fig (21b): Shows the phase diagrams for a) conc of bp = 0.1  $\mu\text{M}$  b) conc of bp = 1  $\mu\text{M}$  c) conc of bp = 5  $\mu\text{M}$

### 3.8 Conclusion

The critical concentration of spermidine (spd+3), cobalthexamine (cohex+3) and spermine (spe+4) needed to condense the DNA molecules are 750 $\mu$ M, 100 $\mu$ M and 6 $\mu$ M. We have shown that DAPI labeled DNA molecules can be condensed at lower concentration of spermidine when compared to YOYO-1 intercalated DNA molecules. By changing the concentration of the DNA molecules we find that there is no change in the critical concentration of spermidine needed to condense the DNA molecules. Therefore critical concentration of spermidine needed for the phase transition remains constant irrespective of the concentration of the base pairs, indicating that this can be an intrinsic variable that depends on the polyamine

### 3.9 References

- [1] J.D Watson et al, *Molecular Biology of the Gene*, 4th ed.; The Benjamin/Cummings Publishing Company, Inc.: Menlo Park, CA, 1987.
- [2] Lerman, L. S. *Proc. Natl. Acad. Sci. U.S.A.* 1971, *68*, 1886.
- [3] Laemmli, U. K. *Proc. Natl. Acad. Sci. U.S.A.* 1975, *72*, 4288.
- [4] Chatteraj, D. K.; Gosule, L. C.; Schellman, J. A. *J. Mol. Biol.* 1978, *121*, 327.
- [5] Post, C. B.; Zimm, B. H. *Biopolymers* 1982, *21*, 2123.
- [6] Widom, J.; Baldwin, R. L. *Biopolymers* 1983, *22*, 1595.
- [7] Murphy, L. D.; Zimmerman, S. B. *Biochim. Biophys. Acta* 1994, *1219*, 277.
- [8] Bloomfield, V. A. *Curr. Opin. Struct. Biol.* 1996, *6*, 334.
- [9] Tabor, C. W.; Tabor, H. *Annu. Rev. Biochem.* 1984, *53*, 749.
- [10] Porter, C. W.; Bergeron, R. J. *Science* 1983, *219*, 1083.
- [11] Hung, D. T.; Marton, L. J.; Deen, D. F.; Shafer, R. H. *Science* 1983, *221*, 368.
- [12] Bloomfield, V. A.; Wilson, R. W. *Polyamines in Biology and Medicine*; Morris, D., Marton, L. J., Eds.; Marcel Dekker, Inc.: New York, 1981; Chapter 10.
- [13] Braunlin, W. H.; Strick, T. J.; Record, M. T., Jr. *Biopolymers* 1982, *21*, 1301.
- [14] Vertino, P. M.; Bergeron, R. J.; Cavanaugh, P. F., Jr.; Porter, C. W. *Biopolymers* 1987, *26*, 691.
- [15] Baeza, I.; Ibañez, M.; Wong, C.; Chávez, P.; Gariglio, P.; Oro, J. *Origins Life Evol. Biosphere* 1992, *21*, 225
- [16] Bloomfield, V. A.; Ma, C.; Arscott, P. G. Macro-Ion Characterization from Dilute Solutions to Complex Fluid; Schmitz, K. S., Ed.; American Chemical Society: Washington, DC, 1994; Chapter 15.
- [17] Pelta, J.; Livolant, F.; Sikorav, J.-L. *J. Biol. Chem.* 1996, *271*, 5656.

- [18] Manning, G. S. Q. Rev. Biophys. 1978, 11, 179.
- [19] Cruz, M. O.; Belloni, L.; Delsanti, M.; Dalbiez, J. P.; Spalla, O.; Drifford, M. J. Chem. Phys. 1995, 103, 5781.
- [20] Rouzina, I.; Bloomfield, V. A. J. Phys. Chem. 1996, 100, 4292, 4305.
- [21] Grosberg, A.; Rabin, Y.; Havlin, S.; Neer, A. Euro phys. Lett. 1993, 23, 373.
- [22] Grosberg, A. Yu; Khokhlov, A. R. Statistical Physics of Macromolecules; AIP Press: New York, 1994.
- [23] Widom, B. J. Phys. Chem. 1996, 100, 13190.
- [24] Vasilevskaya, V. V.; Khokhlov, A. R.; Kidoaki, S.; Yoshikawa, K. Biopolymers 1997, 41, 51.
- [25] Vasilevskaya, V. V.; Khokhlov, A. R.; Matsuzawa, Y.; Yoshikawa, K. J. Chem. Phys. 1995, 102, 6595.
- [26] Mel'nikov, S. M.; Yoshikawa, K. Biochem. Biophys. Res. Commun. 1997, 230, 514.
- [27] Ueda, M.; Yoshikawa, K. Phys. Rev. Lett. 1996, 77, 2133.
- [28] Yoshikawa, K.; Takahashi, M.; Vasilevskaya, V. V.; Khokhlov, A. R. Phys. Rev. Lett. 1996, 76, 3029.
- [29] Yoshikawa, K.; Kidoaki, S.; Takahashi, M.; Vasilevskaya, V. V.; Khokhlov, A. R. *Ber. Bunsen-Ges. Phys. Chem.* 1996, 100, 876.
- [30] Sergio Gurrieri et al Direct Visualization of Individual DNA Molecules by Fluorescence Microscopy: Characterization of the Factors Affecting Signal/Background and Optimization of Imaging Conditions Using YOYO, ANALYTICAL BIOCHEMISTRY 249, 44–53 (1997)
- [41] Yanagida, M., Hiraoka, Y., and Katsura, I. (1983) Dynamic behaviors of DNA molecules in solution studied by fluorescence microscopy. *Cold Spring Harbor Symp. Quant. Biol.* **47**, 177– 187.



- [42]. Bustamante, C. (1991) Direct observation and manipulation of single DNA molecules using fluorescence microscopy. *Annu. Rev. Biophys. Biophys. Chem.* **20**, 415–446.
- [43] Natsuhiko Yoshinaga et al Intercalating Fluorescence Dye YOYO-1 Prevents the Folding Transition in Giant Duplex DNA *Biochemical and Biophysical Research Communications* **286**, 264–267 (2001).
- [44] Nikolay Korolev et al A universal description for the experimental behavior of salt (in)dependent oligocation-induced DNA condensation *Nucleic Acids Research*, 2009, Vol. 37, No. 21 7137–7150
- [45]. Takahashi, M., Yoshikawa, K., Vasilevskaya, V. V., and Khokhlov, A. R. (1997) Discrete coil-globule transition of single duplex DNAs induced by polyamines. *J. Phys. Chem. B* **101**, 9396–9401.
- [46] Yoshikawa, Y., Yoshikawa, K., and Kanbe, T. (1996) Daunomycin unfolds compactly packed DNA. *Biophys. Chem.* **61**, 93–100.
- [47] Widom, J., and Baldwin, R. L.(1983) Inhibition of cation-induced DNA Condensation by intercalating dyes. *Biopolymers* **22**, 1621–1632.
- [48] Toshio Iwataki, Satoru Kidoaki, Takahiro Sakaue, Kenichi Yoshikawa and Sergey S. Abramchuk, (2003) Competition between compaction of single chains and bundling of multiple chains in giant DNA molecules . *Journal of chemical physics*120, **8**, 4004-4011.

## **Chapter 4 DNA in nano-channels**

**4.1 Abstract** In this chapter we aim to study the equilibrium conformation of the DNA molecule in nanoconfinement. For this purpose we fabricated nano-channels of 200nm in width and 300nm in height in PDMS and used fluorescence microscope to observe the elongation of the molecule. Our results show that in 1XT buffer (10mM Tris-Hcl pH=8.5) the elongation of T4 DNA molecule is around 12 $\mu$ m

### **4.2 Extensions of T4 DNA molecules in nano-channels**

Confinement elongation of genomic-length DNA has several advantages over alternative techniques for extending DNA, such as flow stretching or stretching relying on a tethered molecule. Confinement elongation does not require the presence of a known external force because a molecule in a nanochannel will remain stretched in its equilibrium configuration, and hence, the mechanism is in equilibrium. Second, it allows for continuous measurement of length.

Some fundamental statistical mechanical problems are associated with confinement of a polymer in a channel whose width  $D$  is much less than the radius of gyration of the unconfined polymer, such as (i) the dependence of the end-to-end length  $L_z$  of the confined polymer on the length  $L$  of the polymer and (ii) the dependence of the effective spring constant  $k$  of the confined polymer on the length  $L$ . The spring constant sets the scale of end-to-end length fluctuations for the confined polymer because of thermal effects. For the measurement process, an understanding of the relaxation time ' $\tau$ ' is also crucial. A key element for understanding these questions is the influence of

the self avoiding nature of random walk of the polymer in the channel, as we show in Fig. 22.

The effect of self-avoidance on flexible polymers that are freely coiled in solution was first understood by Flory [1] and later generalized to the semi flexible case by Schaefer *et al.* [2]. The rms radius of gyration  $R_g$  of a self-avoiding persistent polymer in solution scales according to Flory–Pincus with the persistence length  $\rho$ , molecule width  $w$ , and contour length  $L$ , such that  $(\rho w)^{1/5} L^{3/5}$ . Compare this form with the result expected for an ideal, non-self-avoiding polymer  $R_g \approx (pL)^{1/2}$ . Thus, self-avoidance for a freely coiled polymer has the following two effects: it adds a weak dependence on the molecule width and it “puffs out” the coil slightly by giving rise to a stronger dependence on the contour length. These equations are, in fact, roughly in agreement with existing data for freely coiled DNA [3]. Benzothiazolium-4-quinolinium dimer (TOTO-1)-dye DNA molecules in the range of 309–4.36 kbp are well fit by the form  $R_g = 80 \text{ nm} \eta [\text{kbp}]^{0.6}$ . Compare this experimentally measured prefactor to the prefactor predicted by the Flory–Pincus result, which turns out to be  $\approx 90 \text{ nm}$  if we use a DNA diameter of 2 nm, a persistence length of 60 nm [4], and a base pair spacing of 0.34 nm [5].

Things change dramatically if the polymer is confined in a channel whose width  $D$  is less than its free-solution radius of gyration  $R_g$ . Self-avoidance increases the scaling exponent for the contour length because the polymer is prevented from back-folding. As de Gennes demonstrated [6], self-avoidance effectively divides the confined polymer into a series of non-interpenetrating blobs, distributing the polymer mass along

the channel in such a way that the monomer density is uniform. Consequently, the extension of the polymer in the channel  $L_z$  must scale linearly with the contour length  $L$ . Assuming that the rms end-to-end length of each blob follows the Flory–Pincus scaling, de Gennes showed that

$$L_z = L \left( \frac{(pw)^{1/3}}{D^{2/3}} \right) \dots\dots\dots(20)$$

this formula gives us a numerical estimate of how much a DNA molecule should stretch in a nanochannel, given that the stretching is purely due to self-exclusion. For example, in a 100-nm-wide channel, we would expect an extension factor, defined as the ratio  $\mathcal{E} = L_z / L$ , of  $\approx 0.20$ ; in a 400-nm-wide channel, we would expect  $\mathcal{E} = 0.15$

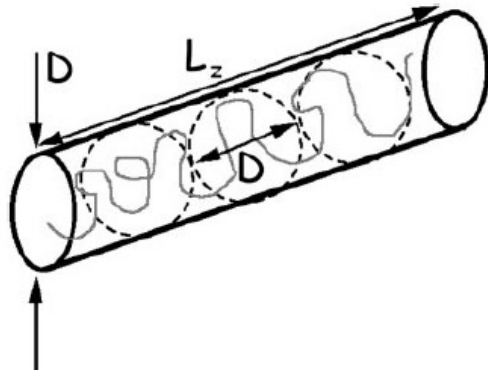


Fig [22]: shows the DNA molecule confined in a channel of diameter  $D$ , the polymer must elongate to some end to end distance  $L_z(D)$ [7]. In a confining tube, the polymer must elongate as a series of blobs which cannot interpenetrate because of self avoidance, thus in a tube diameter  $D$  we should have

$$L_z = L \left( \frac{(pw)^{1/3}}{D^{2/3}} \right)$$

We have investigated the extension of single T4 DNA molecules in 1XT buffer confined in the nanochannels of dimensions 200nmx300nm. Fig. 24 we show the typical

distribution in the extension obtained over 7 individual molecules measured over 300 frames. Due to the photo-bleaching effect of the fluorescence dye, photo damage to the DNA molecule and hydro-phobicity of the chip very few molecules were collected. The average extension of the molecules is about 12  $\mu\text{m}$  which is consistent with the reported results [7-11]. Fig. 23 shows the fluorescence images of T4 DNA confined in nano-channels of cross section 200nmX300nm. It is very clear that DNA molecule becomes more extended once they are confined in the nano-channels. The extension of the DNA molecules increases when either cross section of the channel decreases or the molecular weight of the molecule increases [20, 21].

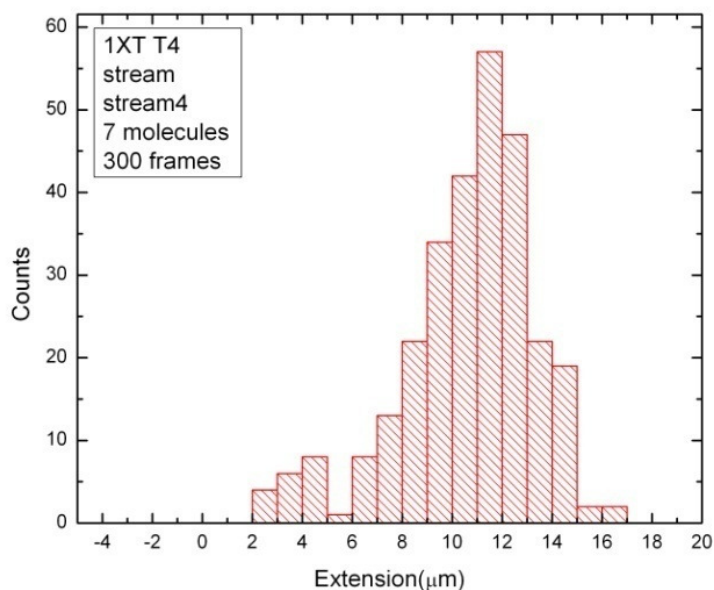


Fig. (23): Distribution of the extension of individual DNA molecules confined in 200 by 300 nm<sup>2</sup> nanochannels. The images were analyzed using Image-J software (<http://rsb.info.nih.gov/ij/>). The DNA molecules are immersed in 1XTbuffer.

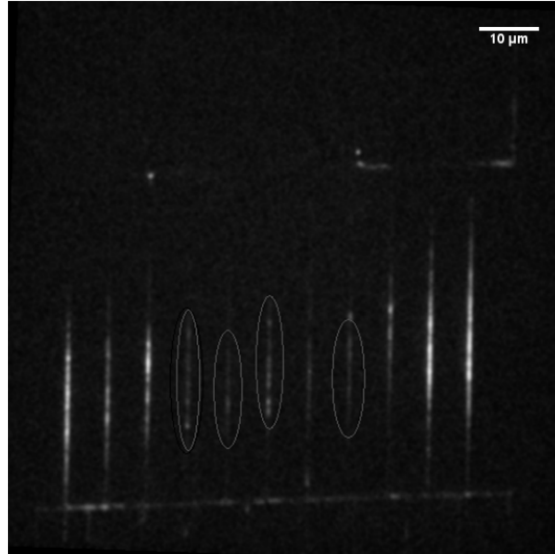


Fig.(24): Shows the Single T4 DNA molecules confined in 200nmX300nm channels. The single DNA molecules are circled.

### 4.3 Translocation of T4 DNA molecules nano-channels

With the technology to make structures on an extremely small scale available, studies of DNA and its various properties in differing conditions in smaller scales have been made possible. In this experiment, the translocation of DNA through small nanochannels is studied. DNA is a negatively charged molecule that is very well affected by the electric field [13]. For DNA undergoing free-solution electrophoresis, the relationship between the DNA's velocity,  $v$  and electric field strength,  $E$  is given as

$$V = \mu E \quad (1)$$

Where “ $\mu$ ” is the Electrophoretic mobility of the DNA molecule [13]. By determining the velocity of the DNA over a range of electric field strength, the linear relationship can be investigated.

## Acquisition and processing

The YOYO-1 stained DNA molecules in the 5XTBE (450mM Tris, 450mM Boric acid, 50mM EDTA) buffer solution were loaded into the 2 reservoirs by injecting the sample solution directly into the chip. Two platinum wires, acting as electrodes, were immersed in the reservoirs and connected to a voltage source power supply (Kethley 237). The movement of the DNA molecules could be controlled via manipulating the electric field, to the extent of causing the DNA to reverse their motion by reversing the field's polarity. The fluorescence of the stained DNA molecules were visualized with an Olympus IX71 inverted fluorescence microscope equipped with a 100 W mercury lamp, a UV filter set and a 100×/1.40NA oil immersion objective.

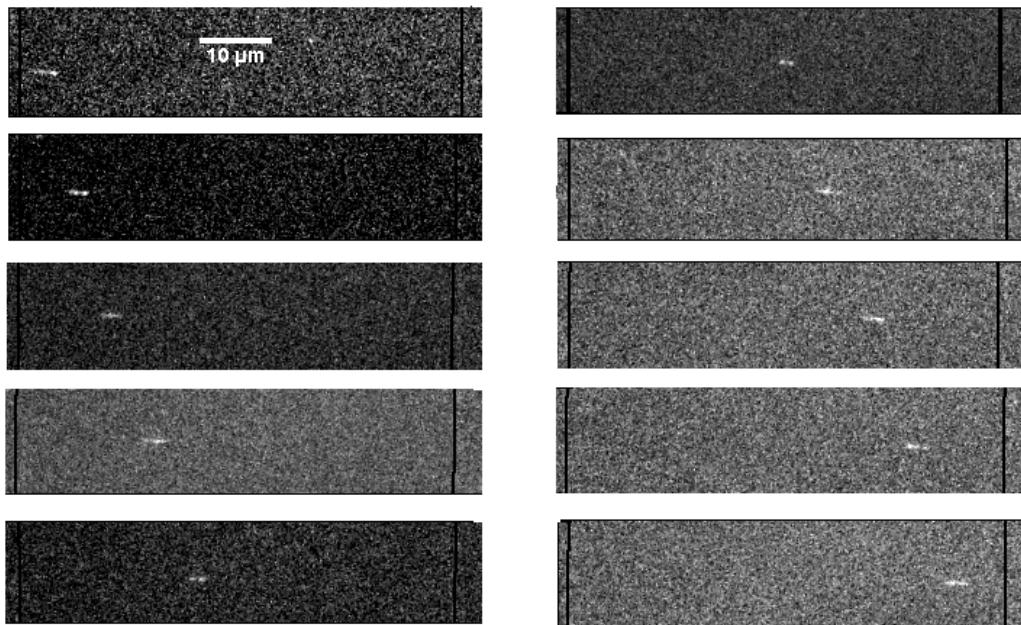


Fig. (25): Sequence of deinterlaced video images showing the passage of a T4-DNA molecule (circled) through a nanochannel. Scale bar = 10  $\mu\text{m}$

The exposure time was controlled by a UV light shutter. Images were acquired with a charge coupled device (CCD) camera (Photometrics Evolve 512, Photometrics, and Tucson, Arizona). Fig. 24 shows the montages of the T4 DNA molecules translocating through the 300nmX300nm channels.

The results obtained from the experiments indicate linear relation between the electric field strength and velocity of the DNA molecule. A graph of velocity against the electric field strength was plotted and a resulting straight line from linear regression was obtained, as shown in Fig. 25. The gradient of the graph corresponds to a mobility of  $\mu = (47 \pm 5) \times 10^{-3} \text{ mm}^2 \text{ V}^{-1} \text{ s}^{-1}$ .

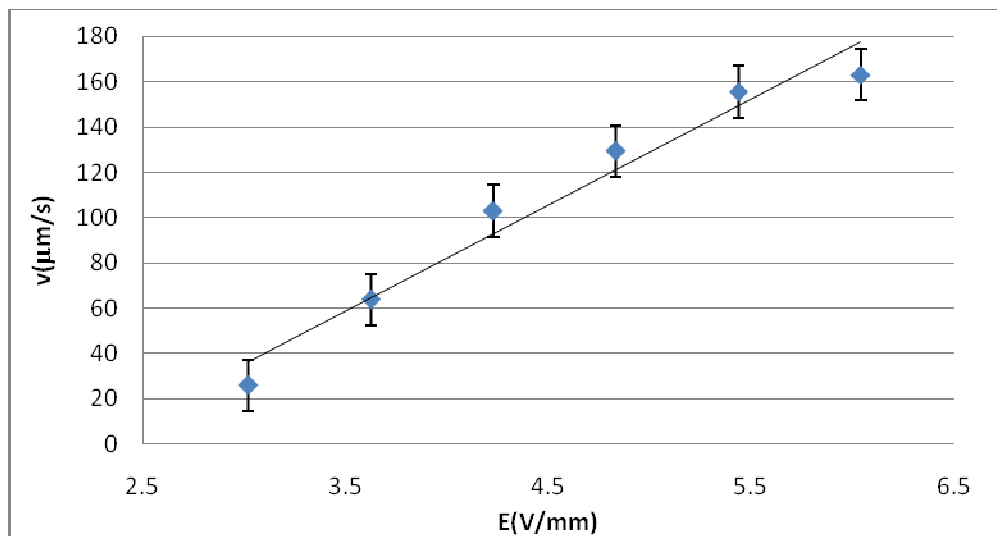


Fig.(26): Graph of velocity vs. field strength. Each point corresponds to the mean of all measurements taken for each voltage. The error bars correspond to one standard deviation.

It is to be noted that below 2 volts of applied potential, no DNA movement into the channels was observed. The reason for this phenomenon is probably due to advection, whereby electro-osmotic motion of the fluid drags the DNA molecule away from the positive pole, and instead brings it towards the negative pole. The electrophoresis effect



on the DNA at voltages below 2 V is not strong enough to compete against the advection of the fluid; hence electro-osmotic flow of the fluid towards the negative pole dominates, preventing the DNA from entering the channels. A chemical known as Polyvinylpyrrolidone (PVP) could be used to suppress the electro-osmotic flow [15], thereby enabling the DNA to enter and translocate through the channels even with the low applied voltage.

At voltages of 5 V and above, the movement of the DNA became too fast so it is difficult to capture with the camera which has a low frame rate. This effect can be seen from the last data point in the graph, which is found to be below the linear fit. Thus for this experiment, the range of velocities that could be tested was limited to the 5 V applied potential which meant that the dynamics of DNA translocating through nanochannels at high speed could not be probed. One method which might help in measuring the high velocities would be to use laser-induced fluorescence spectroscopy to measure the position and speed of the DNA molecules [14].

Another interesting observation made was that the length of the DNA, when translocating through the channels, was increasing in length with increasing applied potential, as shown in Fig. 4. In this case we observed an extension of about 35% of DNA counter length. This increase in length is only caused by the applied electric field [16].

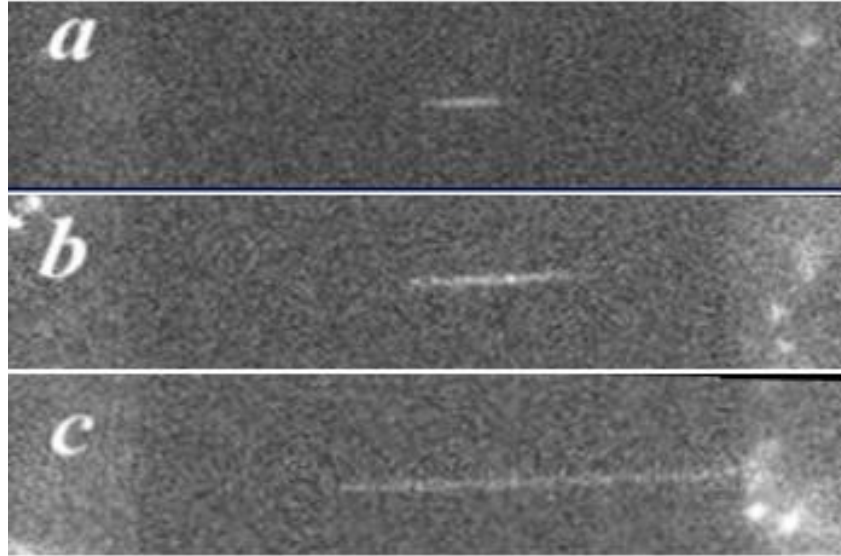


Fig.(27): Captured frames showing the DNA length at different applied potentials, hence velocities. a) applied potential of 2.5V b) applied potential of 3.0V and c) applied potential of 4.5V

#### 4.4 Cross section of micro channels

The cross section of micro-channels was determined by two ways: 1) I-V measurements 2) optical microscope of fractured micro-channels. The micro-channels are 1cm long, 11.5 $\mu\text{m}$  deep and have following widths 8 $\mu\text{m}$ , 12 $\mu\text{m}$ , and 20 $\mu\text{m}$ . Firstly, For I-V measurements the electrolyte used is 1M KCl, 10mM Tris, pH=8.0. The length of the channels is measured using an optical microscope. The area of cross-section is determined from the I-V measurements [17]. All the electrical measurements were done by kethley 2400. Secondly, to measure the dimensions of the micro channel devices optical microscope image analysis of fractured micro-channels cross-section [18] was performed. Sample cross-sectional images of three different types of micro channel systems are shown in Fig. 27. The fractured PDMS micro-channels were prepared by bonding PDMS mould containing micro-channel to another PDMS mould and by cutting in with a blade into PDMS.

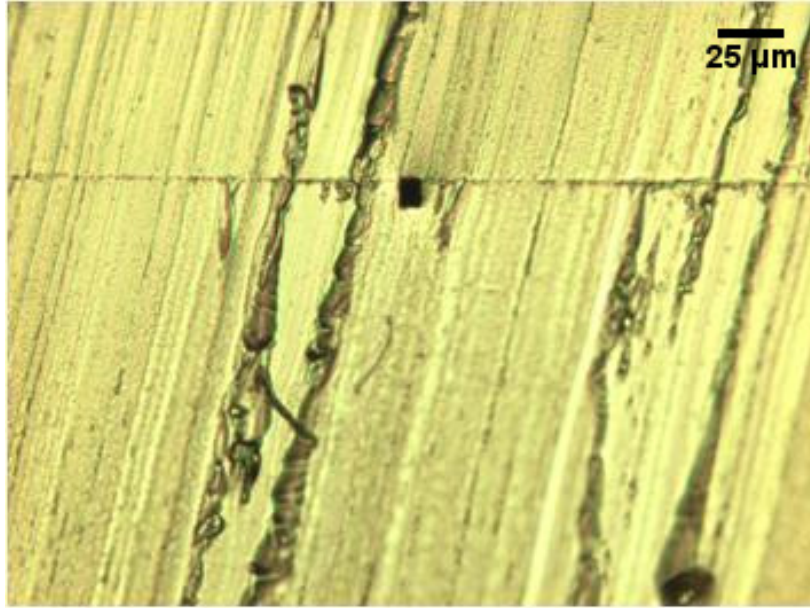


Fig. (28): Optical image of 8-micron width channel. Bonding of a PDMS (mold) to a PDMS (substrate) results in micro channels with a rectangular cross-section.

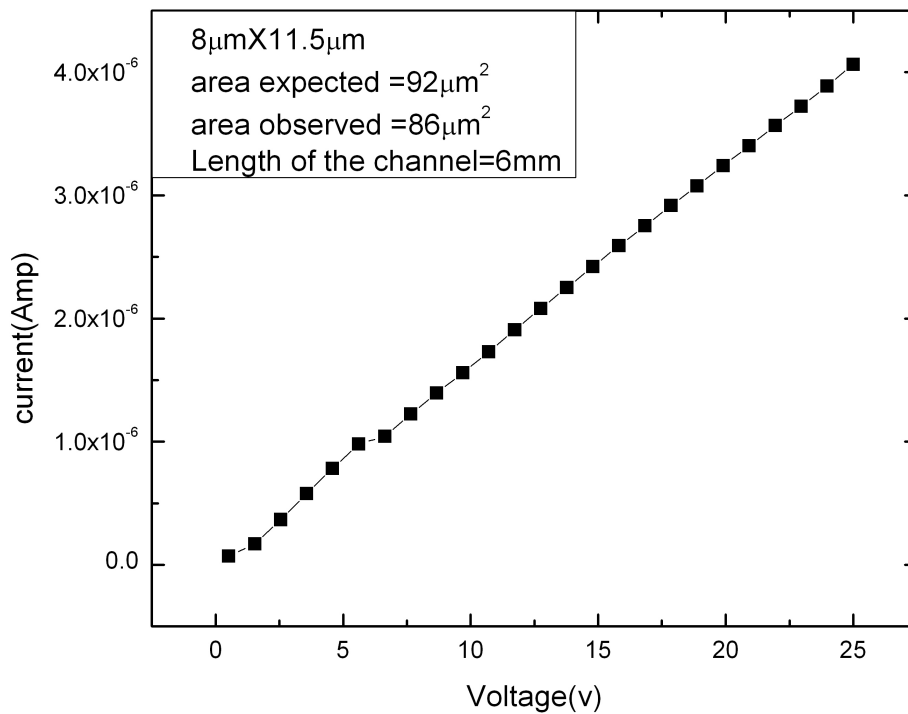


Fig. (29): I-V characteristic of a salt solution (1 M KCl, 10 mM Tris-base, pH= 8.0) along 8 micron width and 11.5 micro meter deep channel.

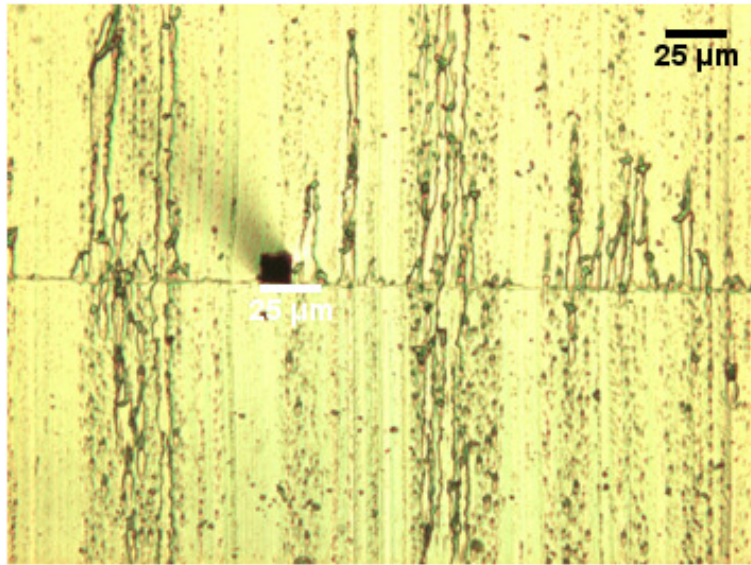


Fig. (30): Optical image of 12-micron width channel. Bonding of a PDMS (mold) to a PDMS (substrate) results in micro channels with a rectangular cross-section

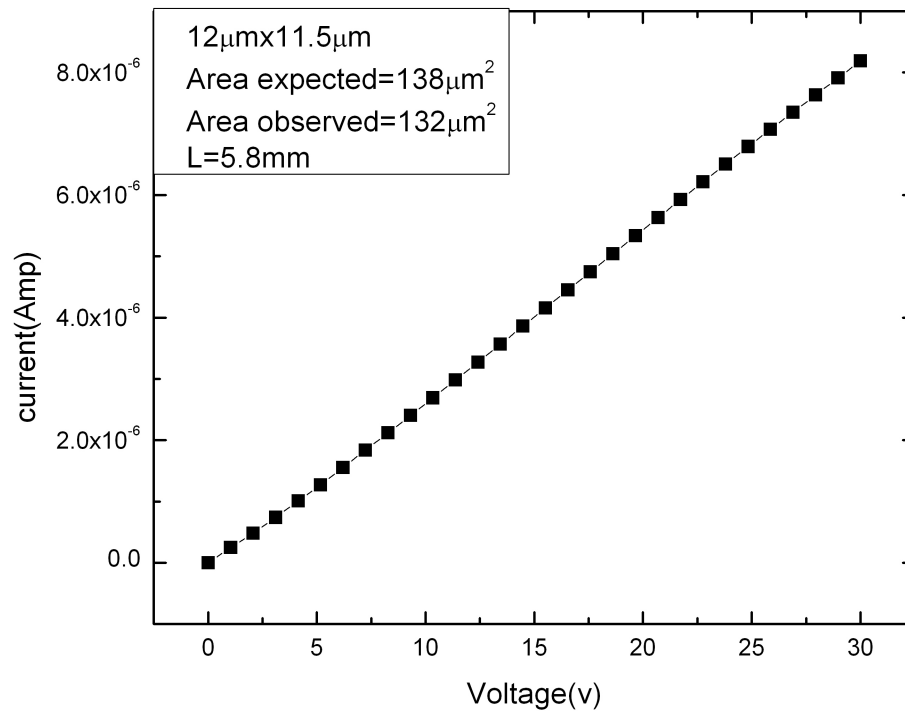


Fig. (31): The I-V characteristic of a salt solution (1 M KCl, 10 mM Tris-base, pH= 8.0) along 12 micron width and 11.5 micro meter deep channel.

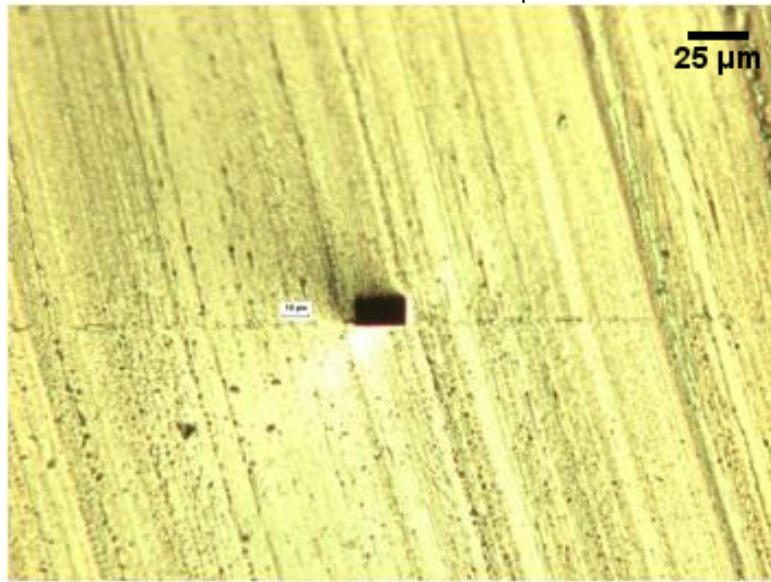


Fig. (32): Optical image of 20-micron width channel. Bonding of a PDMS (mold) to a PDMS (substrate) results in micro channels with a rectangular cross-section.

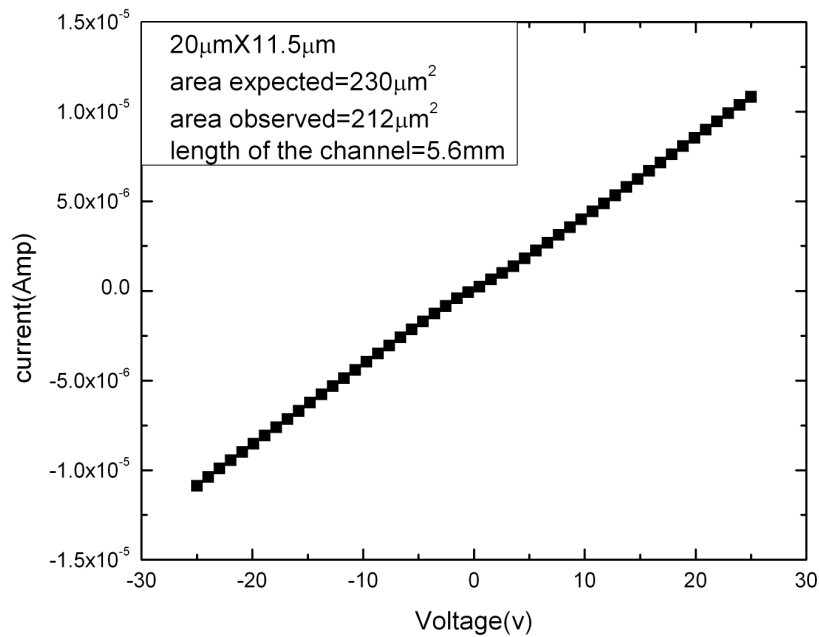


Fig. (33): The I-V characteristic of a salt solution (1 M KCl, 10 mM Tris-base, pH= 8.0) along an 20 micron width and 11.5 micro meter deep channel.

#### 4.5 Cross section of nano-channels

To confirm the 337nmX300nm channel cross-section, we measured the electrical conductance of a salt solution (1 M KCl, 10 mM tris, pH =8.0) along a 337nm wide and 300nm deep 28μm long nanofluidic channel as well as a 5μm wide, 5μm deep, 500μm long microfluidic channel. The total numbers of nano-channels are 11 in between the two micro channels. All electrical measurements were at room temperature using a keithley 2400. Fig. 27, and 28 shows the I-V characteristic in the nano channel, and the area observed is 0.082μm<sup>2</sup> for 337nm wide and 300nm deep channels. In the case of 105nm wide and 100nm deep nano-channel the area observed is 9878nm<sup>2</sup>. The conductivity of electrolyte solution measured with standard conductivity meter is 11.2 S/m. The length of the whole device is 1mm which is measured using an optical microscope. In the below formula  $l_m$  is determined after the reservoirs are punched in the micro channels.

$$R_{Total} = R_M + R_N$$

$$R_T = \frac{\rho l_m}{3A_m} + \frac{\rho l_n}{11A_n}$$

$$R_m = \frac{\rho l_m}{3A_m} = 0.96M\Omega$$

In the above formula we know all the parameter from which we can deduce the area of the cross section of the nano-channels.  $R_T$  is the total resistance of the chip.  $l_m$  and  $l_n$  are length of the micro and nano channels.  $A_m$  and  $A_n$  are area of cross section of the micro and nano channels.

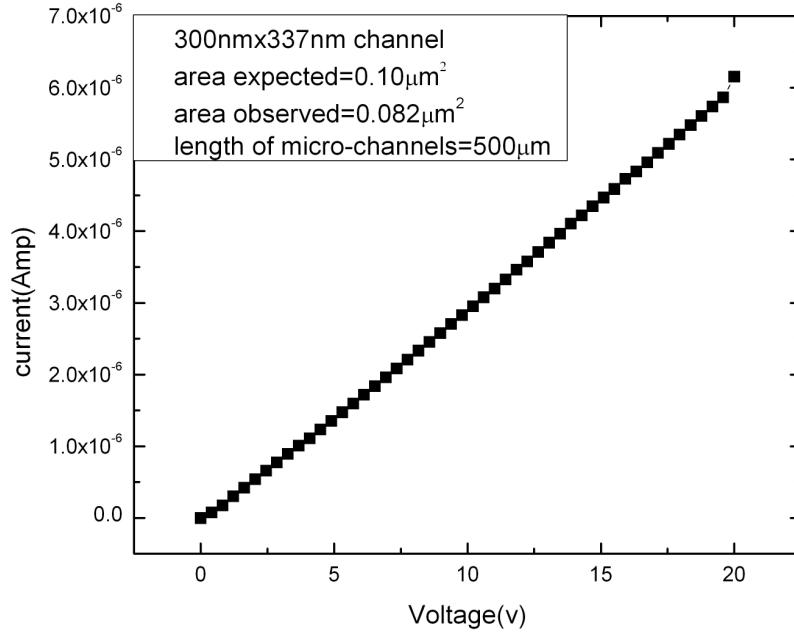


Fig.(34): I-V measurement of 300nmX300nm PDMS nano-channels.

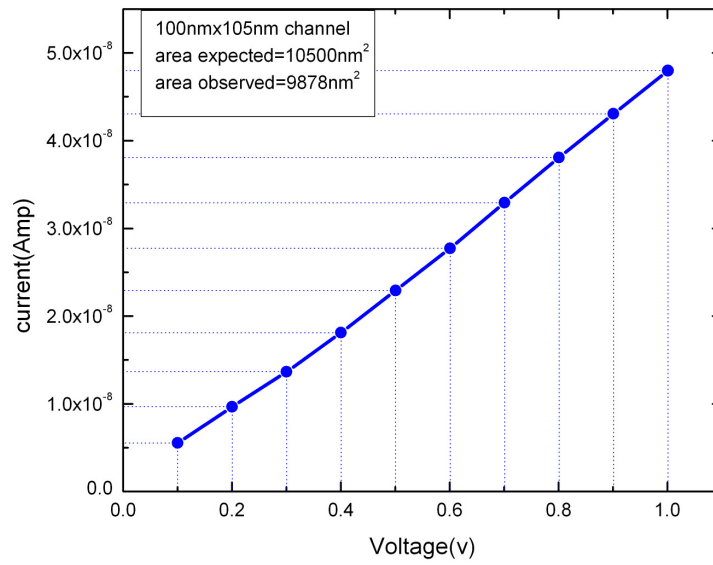


Fig.(35): I-V measurement of 100nmX105nm PDMS nano-channel

## 4.6 Conclusion

The average extension of the T4 DNA molecule in 200nm wide and 300nm deep channels is about 12 $\mu$ m. A linear relationship is obtained between electrophoretic velocity of DNA molecule and voltage in 5XTBE buffer condition. The cross section of the 300nm wide and 300nm deep channels are conformed by I-V measurements.

## 4.7 References

- [1] Flory, P.J. (1953) *Principles of Polymer Chemistry* (Cornell Univ. Press, Ithaca, NY).
- [2] Schaefer, D. W., Joanny, J. F. & Pincus, P. (1980) *Macromolecules* **13**, 1280–1289.
- [3] Smith, D. E., Perkins, T. T. & Chu, S. (1996) *Macromolecules* **29**, 1372–1373.
- [4] Bouchiat, C., Wang, M. D., Allemand, J., Strick, T., Block, S. M. & Croquette, V. (1999) *Biophys. J.* **76**, 409–413.
- [5]. Bloomfield, V. A., Crothers, D.M&Tinoco, I. (2000) *Nucleic Acids: Structures, Properties, and Functions* (Univ. Sci. Books, Mill Valley, CA).
- [6] de Gennes, P. G. (1979) *Scaling Concepts in Polymer Physics* (Cornell Univ. Press, Ithaca, NY).
- [7] Tegenfeldt, J.O., C. Prinz, H. Cao, S. Chou, W.W. Reisner, R. Riehn, Y.M. Wang, E.C. Cox, J.C. Sturm, P. Silberzan, and R.H. Austin (2004). “The dynamics of genomic-length DNA molecules in 100 nm channels,” *Proc. Natl. Acad. Sci. USA*, 101, 10979-10983 [21] Cox, E.C., C.D. Vocke, S. Walter, K.Y. Gregg, and E.S. Bain 1990). “Electrophoretic karyotype for *Dictyostelium discoideum*,” *Proc. Natl. Acad. Sci. USA*, 87, 8247-8251.
- [8] Walter Reisner, Keith J. Morton, Robert Riehn, Yan Mei Wang, Zhaoning Yu, Michael Rosen, James C. Sturm, “Statics and Dynamics of Single DNA Molecules Confined in Nanochannels”, PRL 94, 196101 (2005)



- [9] Walter Reisner, Jason P. Beech, Niels B. Larsen, Henrik Flyvbjerg, Anders Kristensen, and Jonas O. Tegenfeldt, Nanoconfinement-Enhanced Conformational Response of Single DNA Molecules to Changes in Ionic Environment PRL 99, 058302 (2007)
- [10] Diana E. Streng, Shuang Fang Lim, Junhan Pan, Alena Karpusenka and Robert Riehn, Stretching chromatin through confinement, Lab Chip, 2009, 9, 2772–2774.
- [11] Ce Zhang, Fang Zhang, Jeroen A. van Kan, and Johan R. C. van der Maarel, Effects of electrostatic screening on the conformation of single DNA molecules confined in a nanochannel, THE JOURNAL OF CHEMICAL PHYSICS 128, 225109, 2008.
- [12] Chih-Chen Hsieh, Anthony Balducci, and Patrick S. Doyle, “Effects on the Equilibrium Dynamics of DNA Confined in Nanoslits” Nano LETTERS 2008, 6, 1683-1688.
- [13] L. C. Campbell et al Electrophoretic manipulation of single DNA molecules in nanofabricated capillaries Lab chip , 2004 , 4 , 225 –229.
- [14] Christian H. Reccius et al Conformation, Length, and Speed Measurements of Electro dynamically Stretched DNA in Nanochannels Biophysical Journal Volume 95 July 2008, 273–286.
- [15] Takashi Kaneta, Takeshi Ueda, Kazuki Hata , Totaro Imasaka, Suppression of electroosmotic flow and its application to determination of electrophoretic mobilities in a poly(vinylpyrrolidone)-coated capillary, Journal of Chromatography A, 1106 (2006) 52–55.
- [16] Lee BC et al, ELECTRICALLY TETHERED DNA STRETCHING IN NANOCHANNELS, IMECE 2009: PROCEEDINGS OF THE ASME INTERNATIONAL MECHANICAL ENGINEERING CONGRESS AND EXPOSITION, 12, 2010,655-661.
- [17] Xiaogan Liang et al Single Sub-20 nm Wide, Centimeter-Long Nanofluidic Channel Fabricated by Novel Nanoimprint Mold Fabrication and Direct Imprinting NANO LETTERS 2007 Vol. 7, No. 12 3774-3780.
- [18] Seung-min Park, Yun Suk Huh, Harold G. Craighead and David Erickson, A method for nanofluidic device prototyping using elastomeric collapse, PNAS, 106, 37, 15549–15554.

## Chapter 5 Electrolyte top gating of graphene by using micro fluidic channel

5.1 **Abstract:** Graphene is a new class of 2D material with zero band gap, exhibiting a strong ambipolar electric field effect. In this report, we demonstrate the integration of the PDMS micro-fluidic channel with graphene device as a novel way to achieve electrolyte top gating of graphene. By applying a back gate voltage, carrier concentrations of up to  $2.3 \times 10^{12} \text{ cm}^{-2}$  and mobility values of up to  $7500 \text{ cm}^2/\text{Vs}$  can be obtained in the device at ambient conditions. In the case of electrolyte top gating, significantly higher doping concentrations can be achieved as compared to conventional back gating at low voltages. The effective implementation of electrolyte top gating by using micro channels serves as a compelling proof of concept that graphene can be used as chemical and biological sensing.

### 5.2 Introduction

Graphene is a 2D material with a honeycomb structure achieved via  $sp^2$  hybridization of carbon atoms. Since its discovery in 2004 [1], graphene has attracted intense research effort [2]. It has a unique band structure; its conductance and valence bands touch each other at one point, known as the Dirac point making it a zero band gap semiconductor. Carrier types in graphene (electrons or holes) can be continuously controlled globally by means of a back gate voltage, exhibiting strong ambipolar electric field effect [1]. Carrier concentrations of up to  $2.3 \times 10^{11} \text{ cm}^{-2}$  and mobility values of up to  $5000 \text{ cm}^2/\text{Vs}$  can be obtained in our device by back gating.

Although back gating of graphene had been widely investigated, electrolyte gating of graphene still remains to be explored following the successful use of solid polymer top gating by Das et al [3]. Here, we report top gating of graphene integrated with micro-fluidic channel in PDMS. Electrochemical top gating is preferred over conventional back gating using  $\text{SiO}_2$ . This is because higher geometric capacitance can be achieved due to the nanometer thick Debye layer and higher dielectric constant of the electrolyte giving rise to significantly higher doping concentrations [3-5]. For sensing of biological molecules, the ability of graphene to work in an aqueous environment is very important. From the measurements obtained, it demonstrates the attractiveness of graphene not just for electronics but also for chemical and biological sensing in the near future.

### **5.3 Device fabrication and measurement**

Graphene sheets were produced by micromechanical cleavage of highly pyrolytic graphite flakes using scotch tapes [1], followed by deposition of graphene onto p-type Si chip with 280nm thick  $\text{SiO}_2$  on top of it. Preliminary examination of monolayer graphene was conducted via optical microscope, by screening for barely visible regions in comparison to the background colour of silicon chip. It was postulated that the  $\text{SiO}_2$  layer produces a feeble interference-like contrast with respect to the empty Si substrate, which enables identification of graphene [5]. The oxide layer also functions as dielectric layer in back gating. An image of graphene under optical microscopy is shown in the Fig. 36a. Further analysis of the silicon chip for confirmatory presence of single layered graphene sheet would be done by Scanning Tunneling Microscopy (STM) and Raman spectroscopy [6].

Thereafter, a thin layer of polymethylmethacrylate (PMMA) was spin coated on top of graphene as a resist layer. Alignment marks of equal spacing are placed onto the silicon chip to serve as coordinate points Fig. 36b. Based on the location of single-layered graphene relative to the alignment marks, a graphene device was constructed using software Design CAD, in which the layout and precise location of electrodes on graphene are accurately outlined Fig. 36c. The source and drain electrodes (Au/Cr) were then patterned onto the silicon chip by thermal deposition after e-beam lithography. It is necessary for the electrodes to be positioned strategically to avoid obstructions by thicker layer graphite in order to have unambiguous resistivity measurements.

Subsequently, PMMA resist was removed via a lift-off process using acetone (Fig. 36d). Fluidic channels, which were prepared with polydimethylsiloxane (PDMS) mould, with dimension of  $8\mu\text{m} \times 11.5\mu\text{m} \times 1\text{cm}$  were aligned across the graphene sheet (Fig. 36e). Liquid electrolyte, consisting DI water was injected into the gaps situated at both ends of the channel using a syringe needle. Top gating was achieved via insertion of platinum electrodes in the fluidic channel. A diagram of graphene device used in the experiment is shown in Figure 37. Resistance versus gate voltage measurements were conducted at ambient temperature using Lock-In Amplifier SR830 (Stanford research systems), coupled with Keithley 6430 and Keithley 4360.

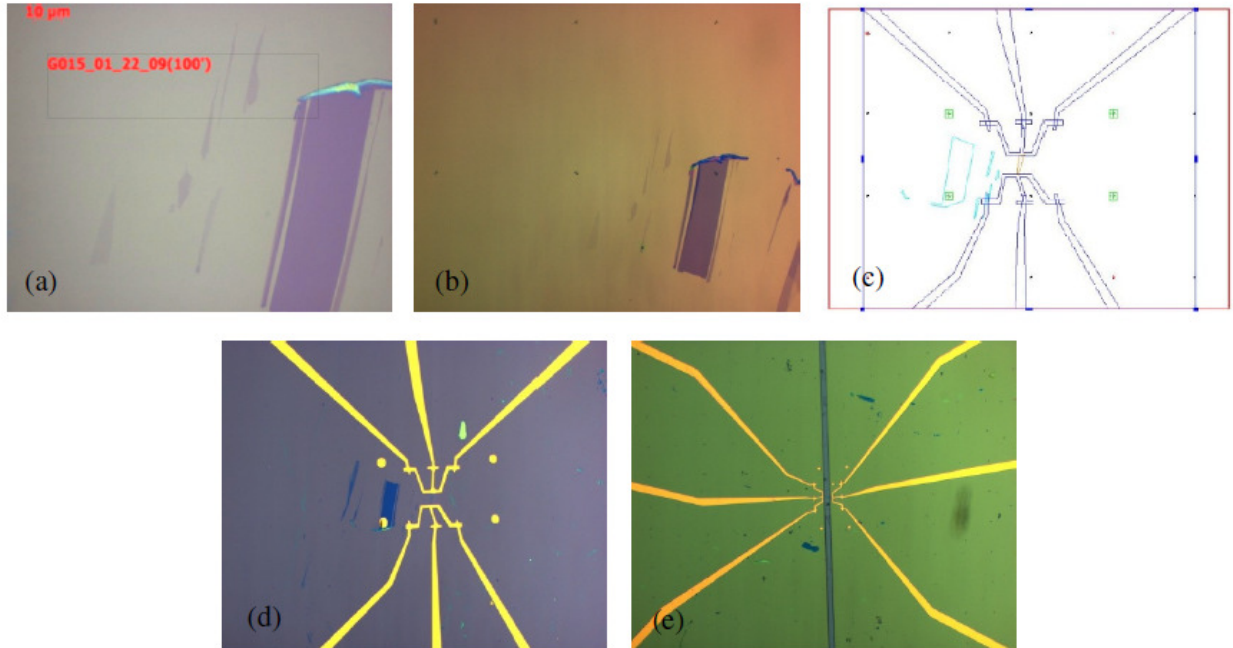


Fig.(36) : (a) View of graphene sample on top of silicon substrate via optical microscope, at 100x magnification. The light purple regions are considered as monolayer graphene, while the area which possesses darker shade of purple is trilayer graphite. (b) Graphene sample observed after spin-coating and placement of alignment marks, viewed in at 50x magnification. The small black dots seen on top and middle are the alignment marks. (c) Image of graphene device, designed via DesignCAD software. Red, dark blue and light blue colored shapes denote graphene, electrodes and graphite respectively. (d) Graphene device shown after thermal deposition of Au/Cr electrodes (yellow) and lift-off, observed at 20x magnification. Large electrodes of average width 25 $\mu$ m connect external voltage source to small electrodes of average width 5 $\mu$ m, which are localized to connect to graphene. (e) The fluidic channel (grey) made of PDMS mould was aligned across graphene. The image was viewed at 10x magnification.

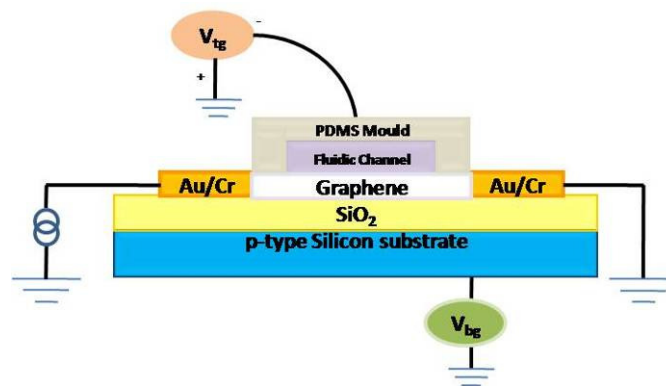


Fig. (37): Schematic diagram showing cross sectional view of electrolyte top-gated measurement device. NaCl solution is passed through in the fluidic channel.

Investigation on graphene for top and back gating experiments require transport measurements. Here we use the standard lock-in technique, which enables the detection of low input signal in the presence of high background noise level. A block diagram of the lock in amplifier is shown in Fig. 3. The amplifier generally functions by synchronizing voltage input signal from the graphene device with a reference signal. In this context, the phase sensitive detector multiplies both input and reference signal of exact frequency and phase difference, resulting in strengthening of input signal, while simultaneously suppressing the noise level [7]. The low pass filter removes the background signal, allowing input signal to pass through and detected as output. Hence, the voltage signal from the device accounts for the majority of output signal. Top gate voltage ( $V_{tg}$ ) was varied between -1 and 1V while back gate voltage ( $V_{bg}$ ) was swept between -6 and 30V. Source and drain current was maintained at 10nArms.

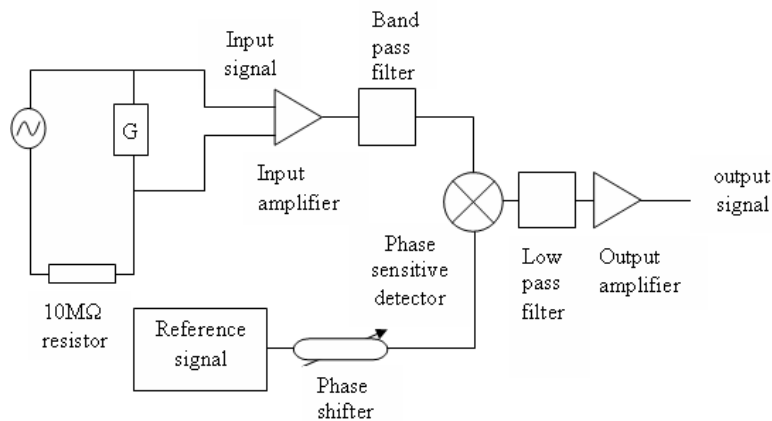


Fig. (38): Diagram showing how current bias transport measurements were conducted. The graphene device (G), connected in the circuit, provides the input signal to the amplifier. The Lock-In amplifier increases the signal input, while filtering background noise signal away from appearing as output signal.

## 5.4 Back gating

The electric field effect refers to the ability to control electronic properties of a material by an electric field by means of a gate voltage. Graphene exhibits a strong ambipolar electric field effect in which both carrier type and concentration can be controlled continuously by applying a gate voltage. In this back gating experiment, we fabricated a graphene device using the methods as mentioned in the device Fabrication and measurement section.

The observed curve is characteristic of single layer graphene, where the plot of resistance against gate voltage is symmetrical with a peak value seen at the Dirac point. As seen from Fig. 5, the peak in resistance of 4k $\Omega$  occurs at V=14V, which is the Dirac point. To the right and left of the peak, the resistance decreases rapidly below 4k $\Omega$ . This is because resistance varies inversely with the charge carrier concentrations (n). The fast decrease of resistance with gate voltages greater or less than 14V implies the rapid increase in charge carrier concentrations. The relationship between the gate voltage supplied and n is given by  $n = \epsilon_0 \epsilon V_{bg} / de$  where  $\epsilon_0$  and  $\epsilon$  are the permittivity of free space and SiO<sub>2</sub> respectively ( $\epsilon = 4$ );  $V_{bg}$  is the applied back gate voltage; d is the thickness of SiO<sub>2</sub> layer which is approximately 280nm and e is the electronic charge. In short, since  $\epsilon_0 \epsilon / de$  is a constant given approximately by  $7.1 \times 10^{10}$ , the above expression is reduced to  $n = \alpha V_{bg}$ , where  $\alpha$  is given by  $7.1 \times 10^{10}$ . By simply applying a gate voltage to graphene, its carrier type can be tuned continuously at doping concentrations of up to  $2.3 \times 10^{12} \text{ cm}^{-2}$ . However, in ordinary semiconductors, the doping level is fixed. In this way, graphene is superior over ordinary semiconductors since carriers can be tuned continuously.

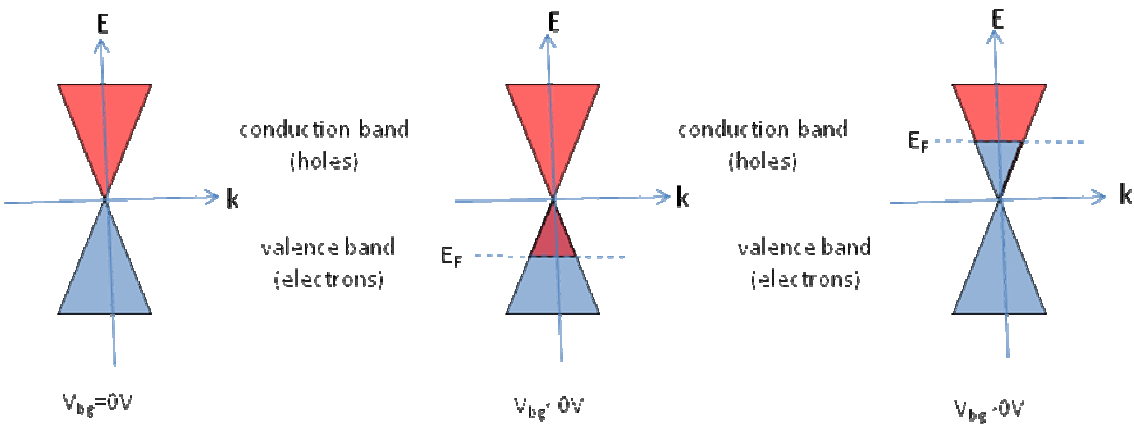


Fig. (39): Energy spectrum in graphene. At 0K, without gate voltage, there is no net concentration of charge carriers. Positive (negative) gate voltage decreases (increases) the Fermi energy, thus creating an excess of electrons (holes) as the charge carrier in graphene.

From Hall Effect measurement, it is known that carriers in the left and right of the peak are holes and electrons respectively. This can be understood as a consequence of shifting the Fermi energy  $E_F$  by an applied gate voltage. An applied negative gate voltage will shift the Fermi energy downwards and vice versa. This results in the excess of holes as compared to electrons hence the carrier in graphene is holes at gate voltages less than 0V. The situation is reversed when a positive gate voltage is applied.

As seen in Figure 4, the peak of resistance known as the Dirac point occurs where the net carrier concentration is zero at 0K. However, the resistance of the device does not go to infinity but reaches a peak of 16k $\Omega$  as there are always some electrons

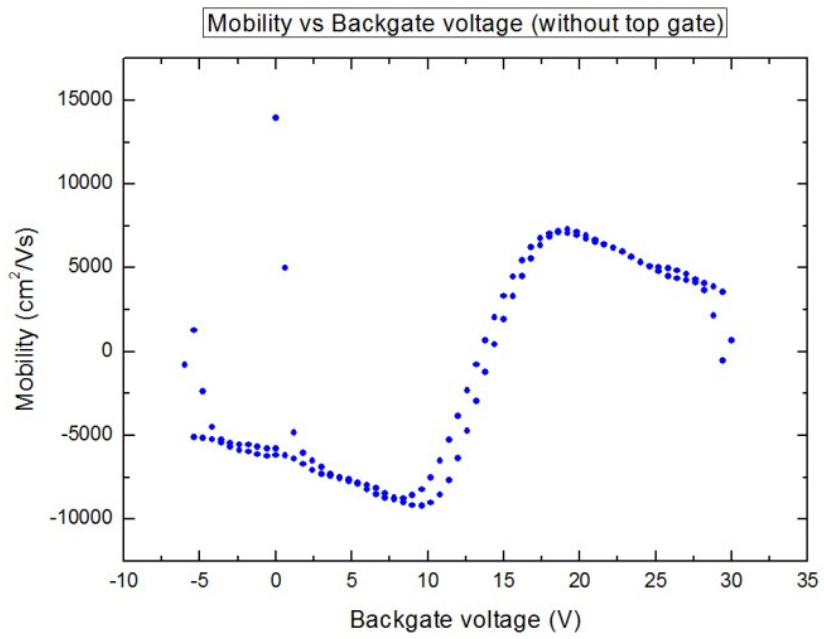
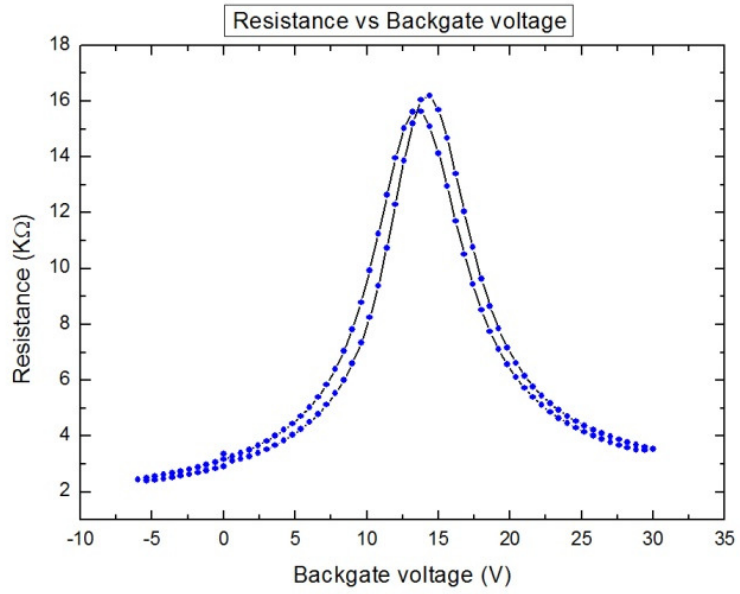


or holes available due to Klein tunneling [7]. In our device, at zero gate voltage (no electric field doping), carriers in graphene are holes while the Dirac point is shifted from 0V to 14V. In other words, it is initially a p doped semiconductor. The reason is due to the unintentional presence of impurities (moisture) in graphene during fabrication, storage and handling of the device. In fact, it has been found that by annealing the device in vacuum, we can shift the resistance peak back to 0V, and exposure of clean graphene to water vapour or NH<sub>3</sub> results in a p doped or n doped device [1].

Given that  $n = \alpha V_{bg}$  and  $\sigma = ne\mu$ , combining these 2 equations we get  $\sigma = \alpha V_{bg} e\mu$  -- (1). Differentiating (1) by  $V_{bg}$ , we get the  $\frac{d\sigma}{dV_{bg}} = 7.1 \times 10^{11} e\mu$  -- (2). From (2),

we can now estimate the mobility of charge carrier in graphene using  $\mu = \frac{d\sigma}{dV_{bg}} \left( \frac{1}{7.1E11e} \right)$ . The graph of mobility against gate voltage is given in Figure 5. Here

we see again that mobility values are the highest at voltages greater or smaller than 14V with zero mobility at the Dirac point. It can be seen that relatively high mobility values of up to 5000cm<sup>2</sup>/Vs and high carrier concentrations of  $2.3 \times 10^{11} \text{ cm}^{-2}$  can be obtained from our graphene device. Mobility remains high even at high doping concentrations in graphene indicating the possibility of ballistic transport in graphene.



## 5.5 Top gating using DI water

While back gating offers an easy way to control the type and concentration of charge carriers present in graphene, this led to poorer device performance due to the lower geometrical capacitance of SiO<sub>2</sub> as a back gate. Here, we report the use of liquid electrolyte, DI as a top gate to control the type and concentrations of charge carriers in graphene, with

Fig (40a): shows the resistance of the graphene with respect to the backgate voltage. Fig (40b): shows the mobility of the charge carriers with respect to the backgate voltage.

The applied potential

difference ( $V$ ) between the graphene sheet and the back gate, which shifts the Fermi level ( $E_F$ ) as seen in Figure 3, inducing different type of charge carriers in graphene.  $E_F$  changes with charge carrier concentrations by  $E_F = \frac{\hbar v_F |\sqrt{\pi n}|}{e}$ , where  $v_F$  is the Fermi

velocity given by  $\frac{1}{300} \text{cm/sec}$  at the Dirac point [8]. The relationship between the

applied gate voltage and the induced electrostatic potential difference is given by

$V_{bg} = \frac{E_f}{e} + V$  where  $V = ne / c_{bg}$ , and  $c_{bg}$  is the geometric capacitance of the back

gate. This is where geometrical capacitance plays an important role as in determining

the electrostatic potential difference  $v$  and the effectiveness in changing  $E_f$  to tune the carrier type and concentrations in graphene.

In the case of back gating using SiO<sub>2</sub>,  $C_{bg}$  is related to the thickness of the dielectric layer by  $C_{bg} = \epsilon\epsilon_0 / d_{bg}$  where  $\epsilon$  is the dielectric constant of SiO<sub>2</sub> (~4),  $\epsilon_0$  is the permittivity of free space and  $d_{bg}$  is the thickness of the SiO<sub>2</sub> layer (300nm). Hence for most back gated graphene devices, the geometric capacitance is low at around  $1.2 \times 10^{-8}$  Fcm<sup>-2</sup>. Therefore, for values of  $n$  of around  $2.3 \times 10^{11}$  cm<sup>-2</sup> given by our back gating experiment,  $V$  is much larger than  $\frac{E_f}{e}$  and hence  $V_{bg}$  is approximately equals to  $v$ .

Therefore the doping concentration in graphene is given by  $n = \alpha V_{bg}$  as described previously in back gating. From this equation, it is clear that in order to get high concentration we need to apply very high back voltages. In practice, the magnitude of applicable back gate voltage is limited by the breakdown limit of SiO<sub>2</sub>, which basically means that there is an intrinsic limit to the concentrations of charge carriers that can be induced by using SiO<sub>2</sub> as a back gate. To overcome this limitation we can increase  $C_{bg}$  by either decreasing  $d_{bg}$  or increase  $\epsilon$  or a combination of both. While materials of higher dielectric constant like HfO<sub>2</sub> and ZrO<sub>2</sub> can solve this problem, these materials are be more expensive [9].

As such, liquid electrolyte top gating is explored to increase doping concentrations more effectively at smaller applied gate voltages. This is because in liquid electrolyte top gating high geometrical capacitance can be achieved as a result of the presence of an extremely thin Debye layer as the dielectric material. It can be seen

in the below Fig. 6 the change in the resistance of the device by the application of the top gate voltage between -1v to +1v. We are able to observe higher doping at low voltages in the device.

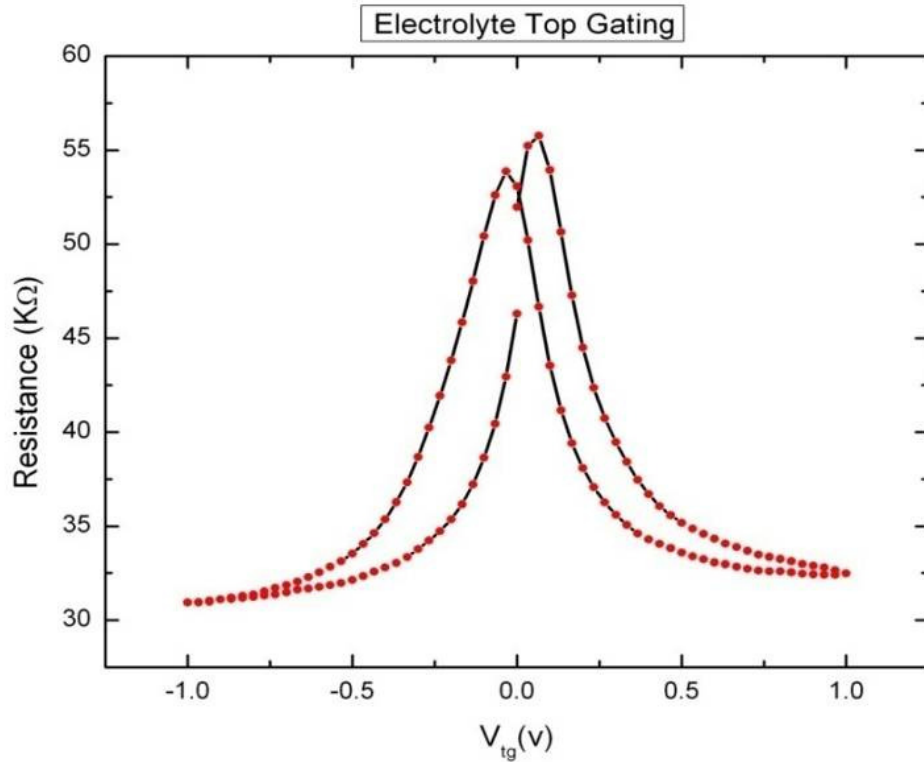


Fig. (41): shows the resistance of the graphene with respect to the top gate voltage from -1v to +1v.

In our experiment, we used DI water as the liquid. It is known that when we apply voltage, free  $H^+$  and  $OH^-$  in the liquid and form a Debye layer on top of graphene. The Debye layer plays the role of  $SiO_2$  layer in back gating. Hence the geometric capacitance of the top gate is given by the similar equation  $C_{tg} = \epsilon\epsilon_o / d_{tg}$  just like before. The thickness of the Debye layer is given by  $d_{tg} = (2ce^2 / \epsilon\epsilon_o kT)^{-1/2} = 2nm$  for monovalent ions  $kT$  is the thermal energy and  $\epsilon$  is the dielectric constant of DI water [3,

4]. Using these parameters, it is determined that the Debye layer of our device is around 2nm which is a significant reduction from 300nm for SiO<sub>2</sub>. Furthermore, since the dielectric constant of DI water is also around 20 times higher than that of SiO<sub>2</sub>, this combination of a higher dielectric constant and thinner dielectric layer led to significantly higher top gate geometrical capacitance of  $7.2 \times 10^{-5} \text{Fcm}^{-1}$ . As described above,

$$V_{bg} = \frac{E_f}{e} + \nu$$

since  $C_{tg}$  is very much larger,  $V$  is no longer very much larger than  $\frac{E_f}{e}$ ,

hence this term cannot be neglected anymore. As such the doping concentrations in liquid electrolyte gated graphene is no longer estimated via  $n = \alpha V_{bg}$  as in back

gating but using 
$$V_{tg} = \frac{\hbar |V_f| \sqrt{\pi n}}{e} + \epsilon \epsilon_o / d_{tg}$$
 Using the calculated values

mentioned above, we reduced the above to  $V_{tg} = 1.16 \times 10^{-7} \sqrt{n} + 2.22 \times 10^{-15} n$  to estimate the doping concentrations in top gated graphene.

By using lower cost materials like electrolytes to significantly improve doping concentrations at lower top gate voltages, we have managed to fabricate graphene devices with better performance.

## 5.6 Future work

The excellent performance of the top gating by using PDMS micro-channel on top of graphene serves as proof that one can achieve electrolyte local gating of graphene [10, -12] by using this device geometry. The work on liquid gating paves the way for future work in realizing graphene based chemical and bio-sensors [13, 14]. A charged molecule near graphene acts in a similar way as ions in the electrolyte as an effective gate to change the resistance of graphene. The large resistance recorded for electrolyte

top gated graphene indicates that a signal from charged biological or chemical species can be readily observable.

## **5.7 Conclusion**

Different types of charge carriers in graphene can be tuned by applying a gate voltage. In this report, we have demonstrated that by using liquid top gating in graphene, we can tune the carriers from electrons to holes. As a consequence, the higher dielectric constant of DI water and the presence of nanometer thick Debye layer leads to higher doping concentrations at smaller top gate voltages as compared to conventional back gating.

## 5.8 References

- [1] Novoselov, K.S. et al. Electric Field effect in atomically thin carbon films. *Science* 306, 666-669 (2004).
- [2] Geim, A.K, et al. The rise of graphene. *Nature Materials* 6, 183 - 191 (2007).
- [3] Das, A. et al. Monitoring dopants by Raman scattering in an electrochemically top-gated graphene transistor. *Nature Nanotechnology* 3, 210 – 215 (2008).
- [4] Rosenblatt, S. et al. High performance electrolyte gated carbon nanotube transistors. *Nano Letters* 2, 869 – 872 (2002).
- [5] Novoselov, K. S. et al. Two-dimensional atomic crystals. *Proc. Natl Acad. Sci. USA* 102, 10451–10453 (2005).
- [6] Ferrari, A. C. et al. Raman spectrum of graphene and graphene layers. *Phys. Rev. Lett.* 97, 187401 (2006).
- [7] <http://www.cpm.uncc.edu/programs/tn1000.pdf>
- [8] Avouris, P., et al. Carbon-based electronics. *Nature Nanotechnology*, 2 605-613 (2007).
- [9] Barbaros Ozyilmaz et al Electronic Transport and Quantum Hall Effect in Bipolar Graphene *p-n-p* Junctions ,PRL 99, 166804 (2007)
- [10] B. Huard et al Transport Measurements across a Tunable Potential Barrier in Graphene PRL 98, 236803 (2007)
- [11] Barbaros Ozyilmaz et al. Electronic transport in locally gated graphene nano constrictions APL, 91, 192107 (2007)
- [12] Biswanath Chakraborty, Anindya Das and A K Sood, The formation of a p–n junction in a polymer electrolyte top-gated Bilayer graphene transistor, *Nanotechnology* 20 (2009) 365203.
- [13] Ang, P. K.; Chen, W.; Wee, A. T. S.; Loh, K. P. Solution-Gated Epitaxial Graphene as pH Sensor. *J. Am. Chem. Soc.* 2008, 130, 14392–14393
- [14] Priscilla Kailian Ang et al, A Bioelectronic Platform Using a Graphene Lipid Bilayer Interface, *ACS Nano*, 4, 12(2010), 7387-7394